

IRIS AND ALMA OBSERVATIONS UNCOVERING A TYPE-II SPICULE AND THE DYNAMIC NATURE OF A CHROMOSPHERIC PLAGE REGION

GEORGIOS CHINTZOGLOU^{1,2}, BART DE PONTIEU^{1,4,5}, JUAN MARTÍNEZ-SYKORA^{1,3,4}, VIGGO HANSTEEN^{1,3,4,5}, JAIME DE LA CRUZ RODRÍGUEZ⁶, MIKOLAJ SZYDLARSKI^{4,5}, SHAHIN JAFARZADEH^{4,5}, SVEN WEDEMEYER^{4,5}, TIMOTHY S. BASTIAN⁷ AND ALBERTO SAÍNIZ DALDA^{1,3,8}

Draft version December 22, 2024

ABSTRACT

We present observations of the solar chromosphere obtained simultaneously with the Atacama Large Millimeter/submillimeter Array (*ALMA*) and the Interface Region Imaging Spectrograph (*IRIS*). The observatories targeted a chromospheric plage region of which the spatial distribution (split between strongly and weakly magnetized regions) allowed the study of linear-like structures in isolation, free of contamination from background emission. Using these observations in conjunction with a radiative magnetohydrodynamic 2.5D model covering the upper convection zone all the way to the corona that considers non-equilibrium ionization effects, we report the detection of an on-disk chromospheric spicule with *ALMA* and confirm its multithermal nature. In addition, we discuss the strikingly high degree of similarity between chromospheric plage features observed in *ALMA*/Band6 and *IRIS*/Si IV (also reproduced in our model) suggesting that *ALMA*/Band6 does not observe in the low chromosphere as previously thought but rather observes the upper chromospheric parts of structures such as spicules and other bright structures above plage at geometric heights near transition region temperatures. We also show that *IRIS*/Mg II is not as well correlated with *ALMA*/Band6 as was previously thought. For these comparisons, we propose and employ a novel empirical method for the determination of plage regions, which seems to better isolate plage from its surrounding regions as compared to other methods commonly used. We caution that isolating plage from its immediate surroundings must be done with care to mitigate statistical bias in quantitative comparisons between different chromospheric observables. Lastly, we report indications for chromospheric heating due to traveling shocks supported by the *ALMA*/Band6 observations.

1. INTRODUCTION

The chromosphere is the most complex and remains one of the least understood layers of the solar atmosphere. It is the layer where the atmosphere transitions from a plasma-dominated to a magnetic-field-dominated regime, it is a medium where ion-neutral interactions matter (such as ambipolar diffusion), and a place in the atmosphere where non-local thermodynamic equilibrium (non-LTE) radiative transfer effects are important. In addition, the chromosphere is the atmospheric shell through which energy and mass from the photosphere must pass in order to heat the overlying corona and power the solar wind.

A major aspect of the physics of the quiet chromosphere is the ubiquitous presence of shocks, propagating

from the photosphere upwards (Carlsson & Stein 1997). Such shocks may play an important role in the heating of the quiet chromosphere. In chromospheric *plage*, i.e., regions of stronger magnetic fields than the typical quiet sun, we find short and dynamic structures called “dynamic fibrils” which are driven by slow-mode magnetoacoustic shocks that propagate from the photosphere to the chromosphere and beyond (Hansteen et al. 2006; De Pontieu et al. 2007a; Skogsrud et al. 2016; Carlsson et al. 2019).

Apart from shocks, several morphological features can be distinguished in the quiet chromosphere; of these the most conspicuous (when seen at the limb) are the so-called *spicules*. They were originally discovered in the 1870s in wide-slot spectroscopic observations in H α by A. Secchi (he called them in French as *petits filets*, i.e., “little strings”, or *poils*, i.e., “fur”, due to their fine and slender appearance; Secchi 1877). Spicules are jets of chromospheric material seen as rooted at the chromospheric network. A new class of spicules, termed as “Type-II spicules”, was found a little over a decade ago in high-resolution imaging observations taken at the Ca II H line (De Pontieu et al. 2007b). These are more slender (apparent widths $\lesssim 1''$) and exhibit higher plane-of-the-sky speeds ($\approx 50\text{--}100\text{ km s}^{-1}$) than their “traditional” counterparts. Their lifetimes differ, depending on whether we observe them in low chromospheric temperatures (e.g., in Ca II H; $\Delta t \approx 10\text{--}150\text{ s}$) or high chromospheric or transition region temperatures (e.g., Mg II h&k and Si IV; $\Delta t \approx 3\text{--}10\text{ mins}$; Pereira et al. 2014; Skogsrud et al. 2016). Type-II spicules have been proposed as contributing to

gchintzo@lmsal.com

¹ Lockheed Martin Solar & Astrophysics Laboratory, Palo Alto, CA 94304, USA

² University Corporation for Atmospheric Research, Boulder, CO 80307-3000, USA

³ Bay Area Environmental Research Institute, NASA Research Park, Moffett Field, CA 94035, USA

⁴ Rosseland Center for Solar Physics, University of Oslo, P.O. Box 1029 Blindern, NO0315, Oslo, Norway

⁵ Institute of Theoretical Astrophysics, University of Oslo, P.O. Box 1029 Blindern, NO0315, Oslo, Norway

⁶ Institute for Solar Physics, Department of Astronomy, Stockholm University, AlbaNova University Centre, SE-106 91, Stockholm, Sweden

⁷ National Radio Astronomy Observatory, 520 Edgemont Road, Charlottesville, VA 22903, USA

⁸ Stanford University, HEPL, 466 Via Ortega, Stanford, CA 94305-4085

the heating of the corona based on observational studies (De Pontieu et al. 2009, 2011). This idea is challenged by low-resolution observations and simplified theoretical approaches (Klimchuk 2012; Tripathi & Klimchuk 2013; Patsourakos et al. 2014) but supported by recent high-resolution observations (Henriques et al. 2016; De Pontieu et al. 2017b; Chintzoglou et al. 2018) and modeling (Martínez-Sykora et al. 2018). Recently, several theoretical models addressed the problem of spicule formation, such as the 3D MHD simulation by Iijima & Yokoyama (2017) where a jet structure (matching the characteristic physical size and life-time of Type-II spicules) was produced and driven by the Lorentz force. Martínez-Sykora et al. (2017) performed a 2.5D radiative MHD simulation (using the Bifrost code; Gudiksen et al. 2011) that considered the effects of ion-neutral interactions in the chromosphere, producing spicules that match the Type-II properties mentioned above.

There has been a controversy regarding the nature of Type-II spicules when seen on-disk, which dates back to the first observations with the *Interface Region Imaging Spectrograph* (*IRIS*; De Pontieu et al. 2014): rapid brightenings along the length of the spicules suggest the upward shooting of hot chromospheric mass at plane-of-the-sky speeds as high as $\approx 300 \text{ km s}^{-1}$ (termed as “network jets”; Tian et al. 2014). Rouppe van der Voort et al. (2015) observed Type-II spicules on-disk and found that the Doppler velocities associated with them were far lower than those seen on the plane of the sky (e.g., Tian et al. 2014). Advanced numerical modeling also suggested that the network jets are often not a manifestation of rapid mass flows but rather rapidly moving fronts of enhanced emission produced by the rapid dissipation of electric currents (e.g., De Pontieu et al. 2017b). In addition, unique observations from a Ly α rocket-borne spectroheliograph, i.e., the Very high Angular resolution ULtraviolet Telescope 2.0 (*VAULT2.0*; Vourlidis et al. 2016), revealed a Type-II spicule in Ly α (plasma temperatures $\approx 10,000\text{-}15,000 \text{ K}$) minutes before such network jets appeared in Si IV imaging ($\approx 80,000 \text{ K}$) from *IRIS* (Chintzoglou et al. 2018). The same work revealed unambiguously the multi-thermal nature of Type-II spicules, since once it appeared in transition region temperatures, the spicule persisted in Ly α imaging, even during the moments of recurrent network jet brightenings.

Recently, the *Atacama Large Millimeter/submillimeter Array* (*ALMA*; Wootten & Thompson 2009) has offered us the possibility to study the chromospheric plasmas thanks to its unique capability in producing high-resolution and fast time-cadence imaging of free-free emission (from chromospheric electrons) in millimetric (mm) wavelengths. Under chromospheric conditions the free-free emission at mm-wavelengths is in LTE and so the source function, S_λ , is the Planckian, B_λ , i.e.:

$$S_\lambda = B_\lambda = \frac{2hc^2}{\lambda^5} \frac{1}{e^{hc/(\lambda k_B T)} - 1} \quad (1)$$

where k_B , the Boltzmann’s constant, h , the Planck’s constant, c , the speed of light, T , the blackbody temperature, and λ , the wavelength of the observations. Since $hc/(\lambda k_B T) = h\nu/(k_B T) \ll 1$ the equation above simplifies to the Rayleigh-Jeans approximation, which is a linear relationship of the source function with the

blackbody temperature. Furthermore, the mm-emission becomes optically thick over a rather narrow width of heights at any given observed line-of-sight in the corrugated chromosphere. Since the emission is optically thick we can use its brightness to determine the local plasma temperature (i.e., at the height of formation of the free-free emission). We thus define the “brightness temperature”, T_b , which is the equivalent temperature a blackbody would have in order to be as bright as the brightness of the observed emission, and which is a measure of the local plasma temperature. Such measurements are enabled via interferometric imaging observations (at a frequency ν) of the spectral brightness, I_ν , translated into T_b through the Rayleigh-Jeans approximation:

$$I_\nu \approx \frac{2k_B\nu^2 T_b}{c^2} = \frac{2k_B T_b}{\lambda^2}. \quad (2)$$

However, since the chromosphere is fine-structured and corrugated, the local conditions producing the optically-thick free-free emission can originate from quite a wide range of geometric heights; the formation height is also dependent on the electron density and thus the actual height where the free-free emission becomes optically thick is typically not well known (Carlsson & Stein 2002; Wedemeyer-Böhm et al. 2007; Loukitcheva et al. 2015; Martínez-Sykora et al. 2020). Therefore, it is not entirely clear for which heights in the atmosphere the local temperature is measured with T_b . In the present paper we are taking advantage of the high spatial resolution *ALMA* observations at $\lambda=1.25 \text{ mm}$ and address the formation height problem for this free-free mm-emission.

Bastian et al. (2017) presented the first comparison between UV chromospheric emission and *ALMA* free-free emission, by exploring how well the T_b measured with *ALMA* at 1.25 mm correlate with the average chromospheric radiative temperatures, T_{rad} , inferred from the average *IRIS*/Mg II h2v and h2r peak intensities, I_λ , with the former obtained by inverting eq. (1) for the temperature as:

$$T_{rad} = \frac{hc}{k_B \lambda} \frac{1}{\ln\left(\frac{2hc^2}{\lambda^5 I_\lambda} + 1\right)} \quad (3)$$

where, c , the speed of light, h , the Planck’s constant, and, λ , the average wavelength position of Mg II h2v and h2r peaks. This study reported a positive correlation with some scatter attributed mainly to the expectation that this relation is not precisely true, since the source function for Mg II h2v/h2r decouples from the local temperature with increasing height in the atmosphere (because Mg II k&h are scattering lines). Similar results were found by Jafarzadeh et al. (2019) using the same *ALMA/IRIS* observations as in Bastian et al. (2018) although they studied correlations between *ALMA*/Band6 T_b with T_{rad} from Mg II but for each of its h and k line features individually. In addition to these works, another interesting application of *ALMA* observations was presented in the study of Yokoyama et al. (2018) and Shimojo et al. (2020), in which they focused on spicules seen at the limb (the latter, however, captured a macro-spicule). These studies faced great challenges due to low signal-to-noise ratio in the *ALMA* limb observations (primarily due to an interferometric “knife-

edge” effect when observing at the limb; Shimojo et al. 2017), also worsened by strong confusion/overlapping from foreground/background structures along the line-of-sight (hereafter, LOS), the latter being typical for observations of spicules at the limb. da Silva Santos et al. (2020) performed inversions of *IRIS* observations and used *ALMA* data as an additional constraint. Apart from several low temperature regions they also found high temperature regions which seem to be associated with shocks pervading the chromosphere. Wedemeyer et al. (2020) presented *ALMA*/Band3 interferometric maps and discussed the potential of such observations for the study of the dynamic chromosphere on small scales (such as small loops).

In this paper, we composed and analyzed a unique and comprehensive dataset from joint observations with *ALMA*, *IRIS*, and the *Solar Dynamics Observatory* (*SDO*; Pesnell et al. 2012). Our dataset is most appropriate for investigating the rich dynamics of the solar chromosphere and transition region in plage and its peripheral areas – such as the study of spicules and chromospheric shocks – thanks to the synergy of high spatial and temporal resolution spectral and imaging observations by *IRIS* with high time-cadence and unique temperature diagnostic capabilities from *ALMA* interferometric observations. Since our results were in strong contrast with those reported by previous studies we perform a thorough comparison to determine the reason behind the discrepancies. For this investigation we introduce a novel empirical methodology to better determine regions of plage in the observations and we employ a state-of-the-art numerical model to synthesize observables for comparison with the observations.

This paper is organized as follows: in § 2 we provide a description of the observations used in this work. In § 3 we present the analysis of the observations and the synthetic observables, and in § 4 our results, followed by a summary and conclusions in § 5.

2. OBSERVATIONS

Our observations targeted a plage region in the leading part of NOAA AR12651 on 22-Apr-2017, centered at heliographic coordinates N11°E17°, or at $(x,y)=(-260'', 265'')$ in helioprojective coordinates (Figure 1a). The polarity of the photospheric magnetic field in that plage region was negative, i.e., of the same sign as the leading sunspot of NOAA AR12651 (Figure 1b). The overall spatial distribution of the plage fields in the target appeared semicircular in shape, as organized around the outer boundary of a supergranule – the latter being evident by the very low magnetic flux density in the core of the supergranule’s area (Figure 1b). The common *IRIS* and *ALMA* field of view (FOV) contained part of that plage, including a photospheric pore, and also intersected the supergranular cell center, which the latter appears in the chromosphere as a region of low background intensity (e.g., Figure 1c). The latter presented us with the opportunity to study morphological structures, such as fibrils or loops, resolved in high contrast due to the weak background emission at the supergranular cell center.

ALMA is a general-purpose ground-based telescope located at an elevation of 5000m in the Atacama desert in Chile, operating in wavelengths ranging from 0.32-3.57mm, or frequencies from 84-950GHz. It includes

two arrays of antennas designed to perform Fourier synthesis imaging together or separately: 1) one array is composed of fifty 12m antennas that can be moved to separations as large as 16km; 2) the other array, the Atacama Compact Array (ACA), is a fixed array of twelve 7m antennas designed for interferometry plus four 12m total power (TP) antennas (see below). *ALMA* was commissioned for solar observing in 2014-2015 and was first made available to the community for scientific observations in 2016 (see Wedemeyer et al. 2016; Shimojo et al. 2017; White et al. 2017). Solar observations use both the fifty-antenna 12m array and the ACA 7m array as a single array. The fifty-antenna array was only available in the most compact *ALMA* antenna configurations (C43-1, C43-2, and C43-3) in 2016-2017 (Shimojo et al. 2017). In addition, pending ongoing commissioning activities, solar observations were initially only available at 3mm (100GHz; Band3) and at 1.25mm (239GHz; Band6). The observations reported here used the *ALMA* C43-3 antenna configuration which provides antenna separations ranging from 14.6m to 500m. The ACA 7m antennas provide antenna spacings ranging from 8.7m to 45m. They were used to image the plage region with an angular resolution of $\approx 0.8'' \times 0.7''$ as determined by the synthesized beam. The array configuration and the beam aspect are summarized in Figure 2. It is important to note, however, that any interferometric array acts as a spatial filter. It does not measure spatial frequencies smaller than the minimum antenna separation in the array, corresponding to the largest angular scales in the source. For the Sun, most of the power is on the largest angular scales and it is therefore important to recover them if photometry is required for the science goals. The 12m TP antennas provide this information by mapping the full disk of the Sun with an angular resolution corresponding to that of a 12m antenna (note that usually, and in our observations, only one TP antenna was used). Roughly speaking, TP maps provide measurement on angular scales $> 24''$ and the joint 12m/ACA array provides measurements on angular scales $< 24''$ for the Band6 observations reported here. The two types of measurements are combined in post-processing using the “feathering” technique (e.g., Cotton 2017).

IRIS is a space-borne imaging spectrograph operating in near-ultraviolet (NUV) and far-ultraviolet (FUV) wavelengths, designed to improve our understanding of the solar chromosphere and transition region. It produces two types of observations: (1) “slit-jaw” context imaging (hereafter SJI) in pass bands centered at Mg II k 2796 Å, C II 1330 Å, Si IV 1400 Å, and Mg continuum 2832 Å; and (2) spectral raster scans (in short, rasters), the latter covering passbands containing several chromospheric and transition region lines found within a NUV and FUV spectral window (range 2783-2834 Å for NUV and two ranges, 1332-1358 Å and 1389-1407 Å for FUV). The rasters are produced at a variety of slit sampling positions, giving the choice of dense ($0''.35$ steps), sparse ($1''$), or coarse ($2''$) rasters in lines like Mg II, Si IV, C II, etc. *IRIS* provided coordinated observations with *ALMA*, starting on 2017-04-22 13:29:36 UT until 16:33:53 UT. The *IRIS* observing mode for this dataset was OBS 3620502035, producing SJI images at the aforementioned passbands at $0''.16 \text{ pix}^{-1}$ with FOV

$60'' \times 65''$ at 13 s cadence and also 16-step dense rasters (i.e., $0''.35$ step in helioprojective x direction and $0''.16$ in y across the slit) covering $5'' \times 60''$ at 26 s cadence of an area intersecting plage, a photospheric pore, and the core of the supergranule (e.g., red rectangle in Figure 1bcd). The spectral resolution in the rasters was 0.025 \AA for the NUV window and 0.05 \AA for the FUV. Since the exposure time was 0.5 s in order to optimize raster cadence for Mg II k spectra, the 1400 \AA SJI images show low signal and have been summed, using a 3-frame (“boxcar”) temporal averaging on the image series. Such averaging improves the signal-to-noise ratio (S/N) enough so as to resolve dynamic features (at an effective timescale of 39 s). Unless otherwise specified in this paper, we do not perform temporal averaging on the raster data since they are of higher S/N.

ALMA observed in Band6 from 15:59 UT to 16:38 UT and produced 5 scans of the target region, owing to four breaks for interferometric calibration (spanning from 1.75 to 2.25 minutes; Figure 2c). In addition, *ALMA* observed in Band3 between 17:20 UT to 17:56 UT but without *IRIS* support. Thus, the overlapping time range between *ALMA* and *IRIS* amounts to a total of 34 mins of Band6 data (Figure 2; Band3 not shown). Within this period of time, *ALMA* was able to capture in ultra-high cadence (2 s) rich dynamic activity and interesting evolution of linear-like structures, including indications for shocks in the region just above the plage. In this work, we focus on the nature of shocks (§ 4.3) and on a slender and dynamically evolving linear-like structure (§ 4.1), resolved with *ALMA*/Band6 observations at high cadence and spatial resolution. In addition, we address the nature of the high correlation we found between spatially-resolved features seen in *IRIS*/Si IV and *ALMA*/Band6 and in other observables both in the observations and in the model (§ 4.2). In the same section we highlight the disagreement between our present work and previous studies that attempted to quantitatively compare chromospheric UV/FUV observables with *ALMA* and we emphasize the deep reasons behind the discrepancies (§ 4.2.1.2, 4.2.1.3, APPENDIX). Here, we propose and adopt a new methodology for the robust determination of regions of plage in order to study the physics of plage free of contamination from other regions with distinctly different physical conditions (§ 4.2.1.1).

3. ANALYSIS

3.1. Reduction of *ALMA* and *IRIS* observations

The calibrated *ALMA* data was obtained from the *ALMA* Science Archive and processed with the Solar *ALMA* Pipeline (SoAP, Szydlarski et al. in prep., see also Wedemeyer et al. 2020 for details). SoAP is developed by the SolarALMA project in Oslo in collaboration with the international solar *ALMA* development team and is based on the Common Astronomy Software Applications (CASA) package (McMullin et al. 2007).

Imaging with SoAP uses the multi-scale (multi-frequency) CLEAN algorithm (Rau & Cornwell 2011) as implemented in CASA, self-calibration for a short time window of 14 s, primary beam correction, and combination of the interferometric data with the TP maps via the “feathering method. For the Band6 observations reported here, the TP maps were scaled to a mean quiet

Sun brightness of 5,900 K as recommended by White et al. (2017), who quote a nominal uncertainty of 5%. For the interferometric part, all frequency channels are used to produce one continuum image for each time step at 2 s cadence. The final result is a time sequence of absolute brightness temperature continuum maps at 2 s cadence with short (~ 2 min) calibration breaks that divide the sequence into 10 min scans.

Ensuring precise co-registration of the feathered *ALMA*/Band6 interferometric maps with the *IRIS* rasters is imperative for the successful analysis of this comprehensive dataset. For this purpose, we used imaging observations in 1700 \AA from the Atmospheric Imaging Assembly (AIA; Lemen et al. 2011) on board *SDO* to coalign *IRIS*/SJI 1400 \AA , 2796 \AA and the FUV/NUV raster image series with other *SDO* observations, such as line-of-sight magnetograms (hereafter, BLOS) produced with the Helioseismic Magnetic Imager (HMI; Scherrer et al. 2012). To coalign *ALMA* with *IRIS*, we exploited the very high degree of similarity between morphological structures seen in *ALMA*/Band6 maps and *IRIS*/SJI 1400 \AA images. This can be readily seen in Figure 1, e.g., by comparing the bottom panels (d) and (e) for bright structures in the plage region. We address the origin of this interesting similarity in § 4.2.

3.2. General Morphology of the Structure Seen in *IRIS* and *ALMA*/Band6 Observations

The *ALMA-IRIS* FOV captured several slender linear-like structures; some of them appeared as persistent and slowly evolving while others showed dynamic behavior over the duration of the observations. In Figure 3 we present a dynamic and prominent linear structure when it first appeared at around 22-April-2017 16:12 UT in the western part of the *IRIS* raster FOV (e.g., see the left group of panels in Figure 3; structure in the *IRIS*/SJI 1400 \AA panel pointed by an arrow). Over the minutes that followed, this structure grew from west to east (e.g., see right group of panels of Figure 3 around 16:17 UT; structure pointed by an arrow). We focus our study on the aforementioned dynamic linear structure in Figure 3 since: (1) its outstanding dynamic nature is interesting; and because (2) for the most part of its time-evolution it is observed against low background emission (due to the supergranular core’s weak magnetic fields; *SDO*/HMI panels in Figure 1 and 3), with the latter allowing us to take measurements that are free of confusion from background structures.

Previous studies on the on-disk counterparts of Type-II spicules identified them through signatures like short-lived asymmetries of chromospheric/transition region spectral lines, which render the lines skewed to the blue or red wing. This effect is described as a “Rapid Blue-shifted (or Red-shifted) Excursion” (RBEs and RREs; e.g., Langangen et al. 2008; Rouppe van der Voort et al. 2015). Here, by exploring the spectral information in the *IRIS* raster series at the corresponding time in the SJI maps of 16:12 UT in Figure 3, we can see that the structure appears faintly in raster images at the blue wing of the Mg II k line, corresponding to Doppler blueshifts of -40 km s^{-1} and also in the Si IV 1393 \AA line, here seen clearly at -22 km s^{-1} (see rasters in left group of panels of Figure 3; dashed semicircle in Mg II k and

Si IV rasters, and in *ALMA*/Band6 common FOV). The structure is not clearly seen in line positions which correspond to Doppler redshifts as high as the blueshifts (see Figure 4 for $\lambda - t$ plots sampling the structure at three different positions across its length). While the evidence is clear in Si IV, Mg II also shows such signature at least in “position B”, albeit with low S/R. As a result we conclude that this feature is characterized as an RBE event. The fact that such slender structure exhibits the spectral signatures of an RBE event further suggests that the linear-like structure is the on-disk manifestation of a Type-II spicule shooting mass upwards (blueshifts of $\approx -50 \text{ km s}^{-1}$ are typical for RBEs associated with Type-II spicules; Rouppe van der Voort et al. 2015; De Pontieu et al. 2017b). Later on, the structure grows further to the east and brightens along its length in Si IV (right group of panels of Figure 3 at 16:17 UT). Throughout the evolution of the linear structure, in the *ALMA*/Band6 data the latter appears somewhat wider and shorter in length as compared to its appearance in the blue wing of Mg II k and in Si IV. However, considering that *ALMA*/Band6 and *IRIS*/Mg II k observations probe similar ranges of temperatures (e.g., Bastian et al. 2017), such differences in morphological structures between Mg II k and *ALMA*/Band6 could be also owing to the difference in spatial resolution between *IRIS* data ($0''.35 \text{ pixel}^{-1}$ in x and $0''.16 \text{ pixel}^{-1}$ in y) and in *ALMA*/Band6 (here, beam size $\approx 0''.7$ at best). Another possibility, despite the common ranges in temperatures in both observables, is that we may not be looking at the same part of the structures as the observed intensities may be coming from different parts of the same multithermal event (see more in § 4.2). In Si IV rasters, different parts of the structure can be seen clearly at -22 km s^{-1} and at $+22 \text{ km s}^{-1}$ away from line center, although the signal in those line positions is lower than at the line core.

3.3. Dynamic Evolution of the Type-II Spicule

In order to properly study the dynamics, we proceed by making an image “cut” in the raster series aligned along the principal axis of the spicule (i.e., its longest spatial dimension; position of “cut” shown in Figure 3 1400 Å SJI panels only for reference as here we focus on the raster series) and produce a space-time plot (hereafter referred to as “ $x - t$ plot”). For our *ALMA*/Band6 observations we make an $x - t$ plot of the brightness temperature, T_b . For *IRIS* Mg II k and Si IV we produce $x - t$ plots in selected wavelength positions sampling the spectral lines around their rest positions, and we stack these $x - t$ plots sorted in the velocity space as shown in Figure 5 (red line marks the time of frames in Figure 3). In the same figure, we also show *IRIS* Mg II k and Si IV $x - t$ plots after integrating the rasters in wavelength (within 0.7 Å and 0.2 Å from line rest positions, respectively). We highlight the parabolic $x - t$ profile of the spicule with yellow dotted lines in Figure 5. The parabola is extracted from the Si IV wavelength-integrated $x - t$ envelope and replicated and overplotted in selected panels of the other observables to serve as a guide for comparisons. The integrated Si IV shows a parabolic profile in a more complete way. In comparison, the profiles in specific wavelength positions appear partial, albeit con-

sistent with Dopplershift modulation due to ascending and descending plasma motions along the evolution timeline. On the other hand, the integrated Mg II $x - t$ profile shows a less clear picture, as we discuss below. Mg II is a complex spectral line that is typically optically thick and formed under non-LTE conditions. Disk counterparts of spicules appear as features that can be both brighter or darker than neighboring features during their complex temporal evolution (e.g., Rouppe van der Voort et al. 2015; Bose et al. 2019). This complex evolution is a key reason for the lack of clear parabolic evolution compared to that seen in Si IV. The structure initially grows from west to east in both the *ALMA*/Band6 and *IRIS* raster plots of Figure 3.

Overall, the behavior seen between these observables is quite similar – for instance, compare the parabolic profiles in the $x - t$ plots of Mg II rest $\pm 27 \text{ km s}^{-1}$ and *ALMA*/Band6, where the trace of the *ALMA*/Band6 emission seems to be co-temporal to similar intensity enhancements in Mg II k. We also note that at Mg II rest -55 km s^{-1} the profile in $x - t$ is more pronounced than that at $+55 \text{ km s}^{-1}$, which is a manifestation of the spicule’s RBE-nature. In fact, the Mg II rest -55 km s^{-1} profile’s duration and elongation corresponds relatively well to the $x - t$ profile in *ALMA*/Band6 up until 16:20 UT (the gaps in the *ALMA*/Band6 observations were due to breaks for calibration purposes).

The Si IV $x - t$ plots (Figure 5; green-colored plots) show upflows during the ascent (or “growth phase”) of the spicule, which is then followed by downflows. The ascending part of the parabolic profile is quite localized (appears as a bright thin trace) and is seen clearly in the blue wing (even seen at a blueshift as high as -66 km s^{-1}). At around 16:16-16:17 UT a network jet brightening occurs in the spicule (dotted circle in Figure 5) with an apparent (i.e., projected on the plane of the sky) speed of $\approx 95 \text{ km s}^{-1}$. Since the time cadence of the rasters was at 26 s this apparent speed is only a lower limit. We note that the network jet brightening started just after the $x - t$ profile’s “apex” point and it is best seen in redshifts, which is consistent with mass motions moving away from the observer. An alternative explanation could be that the spicular column is curved with respect to our line of sight.

We also note an interesting time-dependent intensity anti-correlation between the Si IV and Mg II k $x - t$ plots in these structures: Si IV seems to be brightest where the Mg II is darkest (dotted circles in Figure 5; compare the intensity in the $x - t$ plots between times 16:15-16:20 UT; there seems to be an intensity depression in Mg II $x - t$; more on this in § 4.2).

3.4. Bifrost Simulation of Type-II Spicules and Synthesis of ALMA and IRIS Observables

In order to further investigate the nature of the Type-II spicule, we employ a 2.5D MHD numerical model based on the Bifrost code (Gudiksen et al. 2011), covering the upper solar convection zone all the way to the low corona (extending up to 40 Mm from photosphere). This model includes the effects of non-equilibrium (in short, NEQ) ionization (for hydrogen and helium; Leenaarts et al. 2007; Golding et al. 2016) and ambipolar diffusion (Martínez-Sykora et al. 2017; Nóbrega-Siverio et al.

2020). Martínez-Sykora et al. (2020) compared this model with an equivalent model without NEQ ionization in LTE conditions. The main difference here is that the NEQ ionization increases the electron density, N_e , in the upper-chromosphere due to the large recombination time-scale. In addition, any heating (for instance, due to ambipolar diffusion) or cooling (i.e., due to adiabatic expansion) will increase or decrease the temperature instead of ionizing or recombining the plasma owing to large ionization/recombination time-scales producing multi-thermal structures, such as Type-II spicules or low-lying loops. As we discuss later on, this improves the agreement between synthetic observables and the observations (e.g., as compared to Martínez-Sykora et al. 2017). The spatial scale in the simulation was $14\text{ km (grid point)}^{-1}$. We stored the output of the model at a cadence equivalent to 10 s of solar time. After the simulation relaxed from the initial condition (which took ≈ 50 mins of solar time), the remaining total duration of the simulation we analyze here represents ≈ 10 min of solar time. Using this 2.5D model output we synthesize observables from the physical conditions in the Bifrost model (for each snapshot of the simulation) that correspond to the observed chromospheric emission from a vantage point overlooking the simulation from the top of the domain, essentially simulating “sit-and-stare” slit observations near solar disk center.

The simulation produces Type-II spicules in several locations in the computational domain, in-between regions of emerging flux and plage (the latter containing dynamic fibrils). In order to perform a comparison of the physics and the evolution of the observed spicule with those in the simulation, we focus on a particular region, i.e., at $x = [40, 45]\text{ Mm}$, where two neighboring spicules (hereafter “spicule 1” and “spicule 2”) are seen to develop at a favorable angle with the LOS (e.g., Figure 6ab, annotated and pointed with arrows), which results in well-isolated parabolic profiles in the various $x - t$ plots of synthetic observables presented in Figure 6c-h.

We compute synthetic *ALMA*/Band6 observations from our simulations at a single wavelength position of $\lambda = 1.2\text{ mm}$. For this, we used the LTE module of the Stockholm Inversion Code (STiC code; de la Cruz Rodríguez et al. 2016; de la Cruz Rodríguez 2019). It computes the partial densities of all species considered in the calculations using the electron densities and gas pressure stratifications from the simulation. For the construction of the equation of state (EOS) we use the first 28 elements of the periodic table with 3 ionization stages, except for H. For H we used a simplified EOS that only includes H_2 molecules. Many of those elements will not contribute at mm-wavelengths, but they are included in the opacity and the background opacity (for the latter we consider the partial densities only for elements that are major contributors). Continuum opacities are calculated using routines ported from the ATLAS code (Kurucz 1970), which include the main opacity source at mm-wavelengths (free-free hydrogen absorption; e.g., see Wedemeyer et al. 2016). We also note that free-free and bound-free opacity processes from H and H^- are also included in addition to those for the other atoms considered. The emergent intensity is calculated using a formal solver of the unpolarized radiative transfer equa-

tion based on cubic-Bezier splines (Auer 2003; de la Cruz Rodríguez et al. 2013). The viewing geometry chosen was for an “observer” looking top-down the domain (i.e., assuming a LOS along the vertical direction in the simulation). We show the *ALMA*/Band6 $x - t$ plot in Figure 6c.

In order to synthesize the Mg II k line emission from the simulated spicules we used the Rybicky-Hummer radiative transfer code (in short, RH; Uitenbroek 2001; Pereira & Uitenbroek 2015). The synthesis was done individually for each vertical column of the simulation domain, for an observer looking “top-down” the simulated box (i.e., the z-axis in Figure 6ab). We show an $x - t$ plot in Figure 6e, after integrating Mg II k in a wavelength range of $\Delta\lambda = 0.7\text{ \AA}$ centered at the k3 rest wavelength at 2796.35 \AA (we also show Mg II k spectra in Figure 13).

Lastly, we computed the Si IV 1393 \AA spectrum assuming ionization equilibrium and also assuming optically-thin emission. From the spectrum we compute the intensity by integrating the locally-determined emissivity along the same LOS as before. We thus produced full spectra, which can be used to compare to the *IRIS* Si IV 1393 \AA rasters. An illustration of the Si IV synthesis is provided as an $x - t$ plot in Figure 6g (in this example, we provide the total intensity of Si IV 1393 \AA).

Furthermore, for the optically-thick synthetic observables (i.e., Mg II k, *ALMA*/Band6), we use the height where the optical depth $\tau = 1$ as a function of λ to interpret the diagnostic information we get from the *IRIS* Mg II k and *ALMA*/Band6 optically-thick observations. This quantity is commonly referred to as the *formation height* of a line. For demonstration purposes, here we show the maximum $\tau = 1$ height that the Mg II k has formed at for the wavelength range $\Delta\lambda = 0.7\text{ \AA}$ from its rest wavelength position (Figure 6f). Note that in our discussion we make use of the $\tau = 1$ height also at specific wavelength positions (more in § 4). The Mg II k line includes three components: k2v and k2r form in the wings and originate from the low chromosphere whereas k3, often in absorption, forms in the upper chromosphere. Conversely, Figure 6f reflects that the integrated Mg II k probes the various structures at a range of geometric heights below that maximum $\tau = 1$ height (i.e., it is an upper limit), while *ALMA*/Band6 roughly observes the spicular plasma at consistently greater heights than the wavelength-integrated Mg II k observable (more in § 4).

The optically-thin Si IV synthetic observable captures the basic qualitative behavior of the $x - t$ plot from the observations (Figure 5; green-colored plot), in that it tends to highlight the parabolic profile of spicules 1 and 2. We expand on the similarities seen between the synthetic observables and the observations in the next section § 4. Intensities in *ALMA*/Band6 and Mg II k seem to almost always originate from below that Si IV “envelope”, with *ALMA*/Band6 intensities extending closer to that Si IV envelope than Mg II k. These diagnostics are formed in a region with very strong gradients and very rapid temporal evolution. This means that even though they may be formed in close proximity, they can still be substantially different. To illustrate this point better, we calculate the geometric height of maximum emission for Si IV and we show the resulting $x - t$ plot in Figure 6h. As for the Mg II k line, it forms over a broad range of heights – we

discuss its diagnostic information in comparison to the other observables § 4.2.3

In Figure 7b we present the *ALMA*/Band6 source function, S_ν , calculated separately at each column in the simulated domain, and in Figure 7a the resulting contribution function, g_ν ,

$$g_\nu = S_\nu e^{-\tau_\nu} \alpha_\nu = g_\nu(N_e, T) \quad (4)$$

where α_ν , the monochromatic absorption coefficient, and τ_ν the optical depth for $\nu = 240$ GHz ($\lambda = 1.25$ mm). The source function shows at each column in the domain the range of geometric heights where the (optically-thick) *ALMA*/Band6 free-free emission is forming. The synthetic *ALMA*/Band6 spectral intensity, I_ν , is obtained by integrating the contribution function over the geometric heights along the LOS, z , as

$$I_\nu = \int g_\nu dz = \int S_\nu e^{-\tau_\nu} \alpha_\nu dz. \quad (5)$$

Pairing the above eq. (5) with the Rayleigh-Jeans approximation of eq. (2) we get a map for brightness temperatures, T_b . For comparison, in Figure 7d we show a map of the total (i.e., wavelength-integrated) emissivity for Si IV 1393 Å, $\eta = \int \eta_\nu c / \lambda^2 d\lambda$, with the geometric height where *ALMA*/Band6 $\tau = 1$. This shows that while the total intensity from Si IV,

$$I = \int \eta dz \quad (6)$$

(i.e., in the $x-t$ plot of Figure 6g) may be coming from different geometric heights in the solar atmosphere along the LOS (being optically-thin) – but, nevertheless, delineating the spicules – the *ALMA*/Band6 optically-thick emission comes from a similarly corrugated $\tau = 1$ height (but locally within a small width from that $\tau = 1$ line; Figure 7ab) following closely the height variation of Si IV total emissivity (panel d). Figure 7cd demonstrates that *ALMA*/Band6 provides the temperature at the top part and along the spicules. As for the Mg II k line (not shown in this plot), it forms over a broad range of heights so for reasons of clarity we do not show a $\tau = 1$ line in this figure. Its formation height has strong wavelength dependence as we show in the next section § 4. We discuss the diagnostic information from Mg II k with $\tau = 1$ geometric heights at different wavelength positions in comparison to the formation height of the other observables for spicules and plage in § 4.2.3.

4. RESULTS

4.1. ALMA & IRIS Observations of an Isolated On-Disk Type-II Spicule

The analysis in the previous sections and the qualitative comparison between observational and synthetic $x-t$ plots reveals that our joint *IRIS* and *ALMA* observations have likely captured a Type-II spicule observed on-disk. Figure 4 provides strong evidence of the spicule’s RBE signatures along its slender structure. Also, the dynamic evolution is characterized by upward and downward motions projected in the plane of the sky (e.g., parabolic profile in Figure 5) as also typically seen even for spicules

at the limb. Here, we discuss the similarities in the dynamics of the spicules between the synthetic observables and the observations.

To address the similarities with respect to the dynamic evolution of the spicules, we produce a set of $x-t$ plots at different wavelength positions for the simulated region of spicules (Figure 8) to compare against the $x-t$ plots from the *IRIS* and *ALMA*/Band6 observations which were presented in Figure 5. In addition, we degrade the spatial resolution of the synthetic observables via convolution with the appropriate 2D gaussian kernel to match the observed *ALMA*/Band6 beam size (we pick a “worst beam size” value of $0''.8$) and the spatial resolution of the observed *IRIS* rasters ($0''.16$ pixel $^{-1}$ along the slit). Also, we produce wavelength-integrated $x-t$ plots as done in Figure 5. The qualitative similarities seen in this comparison are striking. We note, however, that the signatures of spicule 2 are not as clear, perhaps because is adjacent to spicule 1, therefore it is not seen against a dark background like spicule 1.

Regarding *ALMA*/Band6, we can see the increase of T_b at the onset of growth of spicule 1 at $(x, t) = (2$ Mm, 3,300 s) and for spicule 2 around $(x, t) = (1$ Mm, 3,300 s - 3,400 s) (display saturated at $T_b = 6,000$ K). In the observations (Figure 5), a similar increase in T_b can be seen to develop at the onset of growth at $\sim 16:10$ UT. Later, at the moment of the network-jet-like brightening in the simulation at $(x, t) = (2$ Mm, 3,650 s), we see an enhancement in T_b (same (x, t) coordinates). Even though in the observations the network jet occurred during the calibration gap between *ALMA*/Band6 Scans 13 and 16, there is evidence that a temperature enhancement was still ongoing at $(x, t) = (3'', 16:19$ UT). Note, however, that we are comparing the observations to simulated events which are not meant to simulate a specific event, therefore differences might be in the details in the simulation, namely, the amount of current, field configuration, etc. Also, the range of values for the synthesized *ALMA*/Band6 T_b for each of the simulated spicules is about 2,000 K lower than the observed *ALMA*/Band6 temperatures in the spicules, suggesting that the energy balance in the simulations does not fully capture all the relevant processes (radiation, heating, ionization, etc.)

To identify the geometric heights where Mg II emission forms in our simulation we use $x-t$ plot of $\tau = 1$ heights as a function of wavelength (Figure 8; each $x-t$ at a specific wavelength and arranged in velocity space). We also plot the parabolic profile for spicule 1 and 2 (yellow and green dotted lines) as taken from the corresponding $\tau = 1$ plots. We typically see that spicules first appear in blueshifts (as high as -37 km s $^{-1}$), which is consistent with the ascending phase in their evolution. Indications for RBE effects are seen in the initial growth phase of the spicules in both Si IV and Mg II k (i.e., see blue oval at -25 km s $^{-1}$ for spicule 1 and at -12 km s $^{-1}$ for spicule 2; compare areas in blue ovals against the red ovals to see difference in intensities). Mg II k progressively samples the spicule at maximum elongation at the line rest wavelength ($+0$ km s $^{-1}$) and in the receding phase of the spicules in the red wing (here, down to $+25$ km s $^{-1}$). In the $x-t$ from *IRIS* observations of Mg II k rest -55 km s $^{-1}$ (shown in Figure 5), we also get signal at the blue wing $(x, t) = (0-3'', 16:10-16:20$ UT).

However, while the $x - t$ plots of $\tau = 1$ in Figure 8 suggest that we are observing the spicule as it grows, stalls and recedes, the Mg II k intensity is (1) too weak and (2) the various contributors to the line too complex in the $x - t$ plot to highlight a rough parabolic profile. We emphasize that this is very similar to what is observed. For instance, see areas pointed by arrows where intensity is low (due to absorption, as we show in the following sections). In the wavelength-integrated map of Mg II k line, we don't see a full (or even partial) parabolic trace as well-defined as in *ALMA*/Band6 and Si IV. The latter is the case for both the observations (Figure 5) and the simulation. Despite that, during the time of the network jet in the simulation, we see significant intensity enhancement at the Si IV rest wavelength all the way to the blue wing (i.e., area inside dotted circle at -25 km s^{-1}) but also indications of Mg II absorption in the red wing (arrow in dotted circle at $+12 \text{ km s}^{-1}$). Likewise, we see similar enhancement from the Mg II k line core to the blue wing in the observed $x - t$ (between times 16:17-16:20 UT).

The most striking resemblance between the simulation and the observations is found in the Si IV $x - t$ (Figure 8). High Si IV emissivity has been observed to emanate from around the tip of the spicule as it grows, until it reaches the apex of the $x - t$ parabolic profile where the emission is then seen mostly at the core of the line (De Pontieu et al. 2017b; Chintzoglou et al. 2018). Remarkably, a network jet brightening here also occurs during the descending phase of the $x - t$ profile (dotted circle in selected panels in Figure 8) and the emission is seen in redshifts (all the way up to $+25 \text{ km s}^{-1}$), as discussed above. Interestingly, the network jet-like brightening appears in Mg II k in blueshifts and also at the rest wavelength of the line but as a *dark feature* in the $+12$ and $+25 \text{ km s}^{-1}$ line positions (compare the dotted circle and locations pointed by arrows). We explore this clear absorption signature in the spicules in § 4.2.

To better illustrate the similarities of the spicule in the model and in the observations, we show in Figure 9 a tri-color combination of the $x - t$ plots that summarize the evolution seen in observations and in the simulation in *ALMA*/Band6 (red), Mg II k, (blue; 0.7 \AA integration), and Si IV (green; 0.2 \AA integration). At the same time this also allows us to assess the instantaneous spatial distribution of the heating along the spicular column. Areas where red, green, or blue, colors produce “color blends” essentially illustrate the multi-thermality of the plasma. In Figure 9a we show the tri-color plot with the *ALMA*/Band6 data gap masking all observables. In panel b we show all available data together with annotations. The tri-color plot from the observations (Figure 9ab) agrees with the general evolution of the simulated spicule 1 and 2 (Figure 9c). Initially (dashed oval A in Figure 9b), the observed spicular plasma only extends to low heights and appears in relatively lower temperatures (no signal in Si IV emission; however, there is signal in both *ALMA*/Band6 and Mg II k at the same location producing a magenta color blend). Eventually, the observed spicular plasma achieves higher temperatures (as also manifested by emission seen in Si IV raster scans; e.g., Figure 5), presumably due to the heating from a shock traveling through the growing spicular col-

umn (thin “linear” bright trace in the $x - t$ plots; Figure 9ab), that leads to both chromospheric and transition region emission. Later on in the observations, shortly after the time when the spicule had reached its maximum elongation, the spicule seems to produce emission in all those wavelength ranges simultaneously. This is marked in Figure 9b with a white arrow as the onset of a network jet brightening. It is worth repeating here that while there is a data gap in *ALMA*/Band6 (dark gap in panel a), there are indications of high signal in *ALMA*/Band6 just after the end of the data gap (bright yellow color blend within dashed oval B). Eventually, as the spicule recedes, significant intensity is found in all three wavelength bands simultaneously (white color blend around 16:22 UT).

The behavior we saw in the observations is also seen in the synthetic tri-color plot for spicules 1 and 2 of Figure 9c; i.e., there is significant intensity at the onset of spicule growth (white dashed ovals A1 and A2 containing the regions with magenta colors), in addition to high emission in Si IV, which here is also seen to “envelope” the parabolic profile of the spicule at all times in the $x - t$ plots. Within the time of the network jet brightening (occurring primarily in spicule 2 but also in spicule 1) high intensity is reached in all these wavelengths (area within dashed ovals B1, B2). Therefore, our synthetic observables (Figure 6) compared to the observations in Figure 5 support the multi-thermal nature of spicules (e.g., Chintzoglou et al. 2018, as revealed by *VAULT2.0* and *IRIS* observations). However, as we mentioned above, the brightness temperatures for the spicule in the synthetic *ALMA*/Band6 observable are $\approx 2,000 \text{ K}$ lower than the T_b in the observations for either of the spicules.

The consideration of time-dependent ionization in the simulation has the effect of increasing the electron density (Carlsson & Stein 2002; Wedemeyer-Böhmer et al. 2007) in chromospheric heights in the domain as compared to previous simulations that did not consider non-equilibrium ionization effects (e.g., see Martínez-Sykora et al. 2020). The above also suggests that, with higher electron densities in the chromospheric plasma, *ALMA*/Band6 (sensitive to free-free emission from chromospheric electrons) is probing spicules in optically thick emission that originates from greater heights due to the increased electron density. This can be seen in the $\tau = 1$ height shown in Figure 7d (red line), which roughly delineates the contour of the spicules; alternatively, compare the parabolic profile in the $x - t$ plot of *ALMA*/Band6 and Si IV (Figure 6c and e). As we already know from previous studies of spicules seen on-disk (e.g., in Chintzoglou et al. 2018) Si IV emission from Type-II spicules roughly demarkates the latter's linear extents as projected on the plane of the sky.

In addition, by including all these effects in the simulation, the simulated spicule 2 (and to some extent spicule 1) suddenly brightens along its full length, producing a network jet. The apparent (i.e., simulated plane-of-the-sky) speed of this network jet is $\approx 140 \text{ km s}^{-1}$, a speed more than 3 times the highest Doppler velocities contained in the synthetic spectra of the spicule at that time (and about 6-7 times higher if compared to bulk plasma speeds in the spicule, which at the time of the network jet are primarily downflows). This mismatch between

apparent speeds and actual plasma speeds (revealed by RBE/Doppler velocities) clearly illustrates the nature of network jets as rapidly propagating heating fronts (De Pontieu et al. 2017b; Chintzoglou et al. 2018), instead of what was previously thought, i.e., rapid upward mass motions (Tian et al. 2014). The similarity between the model and the observations is quite striking and once again points to the impulsive heating and the multithermal nature of spicules (Chintzoglou et al. 2018).

4.2. Understanding the Origin of the Similarities Between *ALMA/Band6* and *IRIS* Observables

The high degree of similarity between *ALMA/Band6* and Si IV observables was discussed in Figure 3 where we also pointed out locations in the FOV where *ALMA/Band6* emission appears in anti-correlation with Mg II k intensity patterns (boxed areas in rasters of Figure 3). In this subsection we perform a quantitative analysis on the degree of similarity between *ALMA/Band6* and other chromospheric and transition region observables from *IRIS*, to better understand the diagnostic potential of *ALMA/Band6* for estimating the temperature of chromospheric plasmas. As we mentioned in § 1, the actual formation height of *ALMA* emission is not well known.

4.2.1. Quantification of Morphological Similarities Between Observables Time-Averaged Over the Entire Image Series

Here, we perform an inter-comparison between wavelength-integrated rasters in Si IV 1393 Å, and C II 1335 Å, Mg II k 2796 Å and also with *ALMA/Band6*.

Comparison between the optically-thick observables *ALMA/Band6* T_b and Mg II is typically done with Mg II expressed as radiative temperature, T_{rad} , in units of temperature [K]. Previous studies (e.g., Bastian et al. 2017, 2018; Jafarzadeh et al. 2019) found that Mg II k2 or h2 lines are highly correlated with mm-emission from *ALMA/Band6* observations, supporting the expectation that *ALMA/Band6* emission forms at mid-to-low chromospheric heights. To compare our study with previous works we perform double gaussian fitting (Schmit et al. 2015) for the Mg II raster data and produce maps representing each feature of the k and h lines, i.e., k2v, k2r, h2v, h2r, k3, h3. We compute T_{rad} with eq. (3) for each of these maps. We also consider the wavelength-integrated Mg II k quantity we produced and used in the previous sections via eq. (3) and get T_{rad} at each wavelength position of the rasters separately (between $\Delta\lambda=0.7$ Å from line center). We then produce the average quantity of T_{rad} representing the wavelength-integrated Mg II k data, by taking the average of T_{rad} produced in that range. The choice of this $\Delta\lambda$ offers the benefit of including all line features of Mg II k (i.e., k2v, k2r, and k3) without extending too much into the line continuum.

For the wavelength-averaged optically-thin observables, computing T_{rad} is physically meaningless and we keep them expressed in intensity units [DN s⁻¹]. For Si IV, the integration was performed for each frame in these rasters in a wavelength range of 0.2 Å. In order to increase the S/N in the C II raster we sum both lines (each centered at 1334.5 Å and 1335.7 Å), and then integrate the sum in wavelength over 0.2 Å. The C II (not

always optically-thick so we keep it in [DN s⁻¹]) rasters suffer from low counts making the presence of hot pixels more impactful in the statistics, with plenty of hot pixels being visible in the map from the average C II image series. We determined that the hot pixels can be extracted easily, since their values exceeded the values from persistent structures owing to real C II signal. Thus, at each frame, we remove any hot pixels exceeding 10 DN s⁻¹ with a mask and substitute values via linear interpolation from values of the immediate neighboring pixels. While significant noise was still present in each frame due to low photon counts, the inspection of the time-averaged map before and after the removal of hot pixels showed that the S/N was improved satisfactorily.

A common approach in multi-wavelength studies utilizing data from different observatories/instruments is to ensure that any time-differences in the image series between different observables are: (1) properly matched/synchronized; and (2) small enough and appropriate for addressing particular science questions. Both are required to effectively “freeze-in-time” the plasma evolution between all the different wavelengths. This becomes a serious concern in studies of the highly dynamic chromosphere, such as the one we report in the present work. Here, we match our *ALMA/Band6* 2 s-cadence series by composing “rasters” that match each slit sampling position to within ± 1 s. We have also performed the analysis presented here by selecting the frame at the time corresponding to the middle of each raster scan (raster cadence 26 s, resulting to ± 13 s time-difference) but found no significant change in our results (i.e., of order $\sim 1\%$). This presents a great improvement as compared to previous studies, where the minimization of time-differences was limited due to the data series used, resulting to a highly variable time-matching between *ALMA-IRIS* observables (i.e., 0.5-2 min). The authors also acknowledge that significant evolution may be ongoing during this period of time between the sampling of the *ALMA-IRIS* observables and also reported findings by a separate analysis where the time difference was strictly chosen to be 0.5 min. However, this constrain, even though it impacted their sample number, it marginally improved the agreement between *ALMA-IRIS* observables. Here, with a maximal difference of ± 1 s we “freeze” the plasma evolution consistently and successfully between each observable over our entire *ALMA-IRIS* image series. However, since the C II rasters have low photon counts, in this section we restrict the comparison between time-averaged rasters over the entire *IRIS-ALMA/Band6* common time series (for a time-dependent study *ALMA/Band6* and *IRIS* Mg II k and Si IV see § 4.2.2). Nevertheless, we fully exploit the excellent synchronization between *ALMA-IRIS* in properly adapting the observables for a thorough comparison (see below).

To perform a fair comparison with *ALMA/Band6*, we degrade the wavelength-integrated raster maps by convolving them with the Band6 beam size and respective position angle at each time frame of our series. Finally, we apply 4-pixel binning along the slit direction for each observable to additionally increase the S/N. The resulting Band6-beam-degraded, time-averaged *IRIS* maps (before and after 4-pixel binning) are shown in the top panels of Figure 10. In the panels before binning (top left) we can see some cosmetic artifacts, namely a dark

line due to the fiducial point which blocks the light in the slit, in addition to a linear-shaped intensity depression (mostly seen in the FUV observables), which appears similar to the shadow casted by the fiducial point. In our analysis, we mask out and exclude these two rectangular areas (see dark bands along the x -direction in the 4-pixel binned maps).

4.2.1.1. Determining and Characterizing Pure Areas of Plage

The chromospheric plage could be defined as the region of high chromospheric intensities above magnetic spatial distributions, with stronger magnetic flux than in the quiet Sun but weaker than that of sunspots and photospheric pores. An observer can determine such areas either (a) “by eye” and cutting out a region manually (e.g., as in Carlsson et al. 2015), or (b) in a quantitative manner, i.e., by selecting a certain intensity threshold for a chromospheric image, or even an area of moderately intense magnetic fields. We note here that for plage regions that appear well-isolated, a “by eye” determination is usually preferred and possibly is accurate if performed with care. However, quantitative methods require human supervision, to ensure that distinct chromospheric features not constituting plage are excluded from plage areas, with a strictness level dependent on the specific science question asked. In other words, if, e.g., we are interested in quantitative comparisons between different observables in plage regions, care must be taken to exclude features that are not classified as plage. That includes: (i) photospheric pores, which may often form sporadically in plage by random convergence of unipolar magnetic fields, or (ii) dark fibrils or other small and cool filamentary structures often seen in the vicinity of sunspot penumbras/superpenumbras. Here we argue that the problem of the definition of plage cannot be solved with the simple choice of thresholds in magnetograms or chromospheric imaging.

Thankfully, our observed plage region was at a safe distance from a sunspot penumbra/superpenumbra (Figure 1a). Thus, to define its boundaries within our small FOV, we could have used a (a) “by eye” determination, or (b) quantitative determination from image segmentation of a Mg II k map (until it matches a “by eye” estimation, e.g., Figure 1f in Bastian et al. 2017), or create a mask from the segmentation of a *SDO*/HMI magnetogram at a moderate threshold value (or range of values) for the flux density (e.g., Figure 5 in Jafarzadeh et al. 2019). Here, however, we produce segmented magnetograms by clipping their values at ± 0.1 kG to quickly distinguish strongly magnetized from weakly magnetized areas. We use the segmented magnetograms as a guide to aid the visual determination of plage from our chromospheric observables. This confirms that the FOV is naturally split into two plage regions (one north and one south in the FOV) separated by a weakly magnetized region. With this in mind and given (i) the several linear-like structures (and spicule) seen in that quieter area, and, (ii) due to the small size of the raster along the x -direction ($5''$) combined with (iii) the knowledge that plage and magnetic fields reside at the west just outside the raster FOV (Figure 1b), we conclude that this middle FOV region is not an isolated “quiet region” but rather a region adjacent to plage, i.e., a region in the

periphery of plage. We also note that the disk location of plage is at sun-center angle of $\approx 20^\circ$ which suggests that we have to be aware of more pronounced systematic offsets between an area defined in the photosphere and its corresponding chromospheric structures. Indeed, in the north plage region of our FOV, while the area is not densely populated by magnetic fields it hosts a multitude of bright structures in the chromosphere, rooted in these magnetic fields. Considering the raster FOV short width ($5''$) and that this north region contains strong magnetic flux elements (and a pore) we treat this region as plage and we isolate these regions “visually” as shown in Figure 10. However, we would like to emphasize that our results and conclusions reported in the following section do not change if we use the segmented magnetogram map as an additional mask, even though the number of points would be reduced (depending on the threshold).

In addition, we employ continuum imaging from *IRIS*/SJI Mg II 2832 Å which clearly shows the existence of a photospheric pore within the north part of the *ALMA-IRIS* FOV. The pore is persistent for the most part of the *IRIS-ALMA*/Band6 common time series. For the exclusion of this area from plage, a choice of a special threshold on a magnetogram map would not be adequate. Here we caution that a larger part of that area in the magnetogram should be excluded, since a thresholded magnetogram at the photosphere is naturally a smaller area than the true area that the magnetic fields occupy at chromospheric heights due to lateral expansion/“fanning” of the field with height. To properly remedy this issue, we employ a *ALMA*/Band6 map segmented at a low threshold $T_b \geq 6,500$ K, to mask the pore out in the chromosphere (note that any of the Mg II, Si IV, or C II from *IRIS* could be used equally well for a choice of threshold; however, since *ALMA*/Band6 maps already pose a limitation due to their irregular resolution element, i.e., the beam, here we produce a mask from Band6 to further restrict the accidental inclusion of lower T_b values in our comparisons due to spatial smearing from the beam). Again, we preferred the use of this mask over the one that could be obtained from, e.g., the *IRIS*/SJI 2832 Å continuum image or from *SDO*/HMI magnetogram (i.e., as done in Jafarzadeh et al. 2019), since the latter does not completely account for the different physical conditions due to the pore’s influence in its immediate plage, e.g., due to the fanning of the strong magnetic field above the pore, which is stronger than the typical magnetic field in plage. In any case, the pore is fully contained within the masked region. The final results can be seen in the top panel of Figure 10, where we overplot on an *SDO*/HMI map the regions of (a) plage (with red and with orange contours showing the extracted area above the pore region), and, (b) its periphery (within a blue colored contour). As we will see in the following paragraphs, the robust determination of plage is extremely critical for carrying out quantitative comparisons between observables.

Therefore, in the present study we consider plage to be the hot magnetic canopy above photospheric magnetic concentrations typical in plage. We have been unprecisely careful to not include other elements such as pores or the superpenumbra from nearby spots (although our observations were taken at a safe distance from the

sunspot near our plage region).

We summarize our definition of plage for chromospheric observables using the following quantities and requirements:

- photospheric magnetogram to be used as a guide (threshold choice at ± 0.1 kG, although similar results can be found for even lower values),
- continuum maps to identify locations of pores within plage or sunspot penumbras,
- chromospheric intensity maps (e.g. Mg II or any other chromospheric observable) also used to remove pores with proper intensity thresholds above identified regions of pores,
- avoid regions of sunspot superpenumbra which typically extend further out than the sunspot penumbra (i.e., staying away from the immediate vicinity of well-developed sunspots)

These criteria help select and safely extract a clean sub-region of plage. As we show in the following paragraphs, when these are not taken into consideration simultaneously, sources of bias appear which lead to discrepancies between our results and previous studies.

4.2.1.2. Quantitative Comparison Between Time-Averaged Observables in Plage and its Periphery—

At first sight, the similarity between C II and *ALMA*/Band6 is striking. We proceed by calculating the linear correlation coefficient (Pearson r , hereafter “C.C.”) between each of the four observables (i) inside the plage region, (ii) inside the region containing the periphery of plage, and (iii) for the full FOV in the rasters mixing together plage with its periphery, first with the presence of the pore (the respective C.C. values for each region are shown within black boxes at the top of each scatter plot). Then we also calculate the C.C. for regions (i) and (iii), after the pore area is excluded in each of the observables (values shown within the dashed orange boxes in each scatter plot). The impact of this low temperature *ALMA*/Band6 region in plage and in the full FOV C.C. can be readily seen in the values presented in the scatter plots in Figure 10abc. The pixels in the region above the pore produce a clear “spire”-like feature or a “tail of points” towards low *ALMA*/Band6 T_b values (i.e., $4,000 \leq T_b \leq 6,500$ K, i.e., our T_b threshold choice for producing the pore mask is fully consistent with representing this feature). Removing those pixels with the application of the pore mask improves the C.C. for the full FOV and plage significantly (red points marked with an orange “ \times ” symbol). However, we caution that the C.C. obtained over the full FOV is not particularly informative since it mixes plage regions with much quieter regions in the plage periphery, i.e., regions with very different physical conditions. Nevertheless, we still provide the results for full FOV as well as the results without the removal of the pore region for completeness. We address the impact of mixing plage areas with other areas with lower temperatures in § 4.2.1.3.

We first focus our analysis and discussion for the plage (excluding the pixels above the photospheric pore) and periphery regions separately and keep the analysis for the

full FOV to link our work to previous studies (§ 4.2.1.3). To facilitate the presentation of the results, in the bottom panels of Figure 10 we organize the various C.C. values from each combination of the observables with the aid of correlation matrices. The correlation matrix for plage shows that C II is highly correlated with all other observables (C.C. ranging 0.73 to 0.79). In contrast to that, the observable with the lowest correlation between observables in plage is Mg II k T_{rad} . *ALMA*/Band6 and Si IV and C II form a triad where the C.C. is the highest. Perhaps this shouldn’t be a surprise, since these high values are fully consistent with Si IV and *ALMA*/Band6 forming close to each other, thus probing similar structures. In addition, we emphasize that the Mg II T_{rad} is averaged over 0.7 \AA so that it mixes information from a wide range of heights. We note that if we use the wavelength-averaged Mg II k time-averaged map expressed in intensity [DN sec^{-1}] instead of T_{rad} in [K] our results in the correlation study we present here do not change beyond a few percent. In addition we emphasize that if we impose thresholded magnetogram masks for the plage areas the results do not change beyond 3-5% which further confirms the robustness of our methodology.

The similarity between C II with Si IV has been mentioned previously in visual comparisons between *IRIS* C II, Si IV and Mg II rasters (e.g., Rathore et al. 2015a). In a study by Rathore et al. (2015b) (e.g., Figure 17 therein), Si IV was found to form consistently higher (having normally a formation height in the transition region, around $T \approx 80,000$ K) than Mg II and C II, although C II was found to form either above or below Mg II k3. However, it was also noted that C II primarily formed above the formation height of Mg II. While these authors did not investigate the formation height of *ALMA*/Band6 in that work, the height of $T \approx 12,000$ K and $80,000$ K is provided in the plot of Figure 17 therein and it seems that C II forms sometimes either above or below that $12,000$ K height. On the other hand, Mg II is consistently lower and in only a few locations coincides with that height. The authors discuss that this is caused by the presence of low density, cool “pockets” of plasma at those heights where density is enough to place the $\tau = 1$ surface for C II at that height. However, the density is not as high for Mg II to form as high as C II. The authors conclude that C II forms higher up in fibril structures in their simulation domain, by also noting that Mg II and C II show, on average, similar patterns in their heights of formation.

Our results in the correlation matrix for plage support this finding, given that C II shows very high correlation with *ALMA*/Band6 and Si IV, the later being understood as all these observables have formation heights relatively close to each other, effectively sampling the conditions along similar parts of structures above plage. Mg II k T_{rad} seems poorly correlated with all other observables but C II, suggesting that C II forms above Mg II k but between Mg II k and *ALMA*/Band6 and Si IV. Again, we emphasize that our average Mg II k T_{rad} used here (corresponding to the wavelength-integrated Mg II k) forms over a wide range of heights than the other observables (however, as we will see in §) 4.2.1.3 it makes little difference if we use Mg II k2v or k2r after extracting the peaks with line fitting). To this we should add that the inter-

esting anti-correlation seen between maps of Mg II k and *ALMA*/Band6 and Si IV in certain locations of the FOV (Figure 3; boxed regions in plage), presumably due to enhanced absorption, may have the effect of weakening the correlation of Mg II k with the other observables. Nevertheless, this does not lead to a contradiction in our interpretation, since the correlation between Mg II k T_{rad} and Si IV in plage is moderate (C.C. = 0.57) and not different from that between Mg II k T_{rad} with *ALMA*/Band6 T_b (C.C. = 0.56).

The correlation matrix for the periphery of plage shows a similar picture. The C.C. between C II and the other three observables remains the highest as compared to any other combination of three particular observables. The significant strength of the correlations with C II for the periphery appears consistent with the results of Rathore et al. (2015b), which place the formation height of C II higher than Mg II and thus closer to Si IV in the fibril regions (Figure 18 therein). Note however that Rathore et al. (2015b) did not average Mg II k over 0.7 \AA . The periphery of plage here contains several linear-like structures, which suggest similar geometry as in the simulations of Rathore et al. (2015b) (e.g., here in Figure 10 see the persistent thread-like structures in the time-averaged maps). On the other hand, this region also exhibits low signal in Si IV and *ALMA*/Band6. This may explain the significantly lower correlation between Mg II, Si IV, and *ALMA*/Band6 as compared to that in plage, since Mg II intensity seems more diffuse in that region. We note that a study of correlations between C II T_{rad} and *ALMA*/Band6 T_b was performed by Jafarzadeh et al. (2019) and also found a high Pearson C.C. of 0.83, although it was mentioned there that the origin of this high correlation with *ALMA*/Band6 was not understood.

4.2.1.3. Understanding the Discrepancies with Previous Studies—

While we find a moderate-to-high correlation between C II, Si IV, and *ALMA*/Band6, the C.C. we find for Mg II and *ALMA*/Band6 lies in the low end of those reported in previous studies. For instance, Bastian et al. (2018) compared T_{rad} of Mg II h to *ALMA*/Band6 T_b and reported a very high, C.C. = 0.80, for plage. There are several differences between our work and that of Bastian et al. (2018). First, the T_{rad} in Bastian et al. (2018) was produced from maps of the average T_{rad} of Mg II h2v and h2r by also including single-peak profiles in those maps. Here, we integrated Mg II k over 0.7 \AA . We note that the observational programs used in the data used in the aforementioned studies did not allow for a good synchronization between the different spectral windows. In the present study the observations were acquired with a less restrictive program that has allowed us to achieve a tighter time coherence among all spectral bands. We also note that the determination of plage was done with different criteria than ours (§ 4.2.1.1), i.e., based on the visual identification of obvious morphological features in the FOV (i.e., contours roughly containing high Mg II h2v and h2r average T_{rad} and T_b for plage; Bastian et al. 2017; Figure 1f therein). Here we employ strict criteria for the definition of plage and its periphery, based on *SDO*/HMI photospheric magnetogram maps with magnetic field values $\geq \pm 0.1 \text{ kG}$ which splits the FOV into a north and a south plage region betwixt a region con-

taining the periphery of plage (as no obvious magnetic elements are seen in that region; Figure 1, and also see green isocontours at $\pm 0.1 \text{ kG}$ in Figure 3 and 10). In addition, we carefully remove the area in plage above a photospheric pore. We focus on a different Mg II spectral line, i.e., Mg II k and we obtained the T_{rad} over 0.7 \AA centered at the rest wavelength of the line (thus the wavelength range is large enough to contain the k2v and k2r peaks but without including the line continuum). However, given the large discrepancy in the C.C. (Bastian et al. (2018) C.C. is 40% larger than our value), we calculated the T_{rad} in the same way as in Bastian et al. (2017) and Bastian et al. (2018) for the average Mg II h2v and h2r line, only to find out that the C.C. in that case is even lower, i.e., C.C. = 0.52, yielding an even larger discrepancy of our results with the results reported in Bastian et al. (2018) (i.e., 54% larger than our value).

Even though the number of pixels available in our *IRIS*/*ALMA* FOV is significantly lower as compared to the much larger raster and *ALMA*/Band6 mosaic of Bastian et al. (2017) and Bastian et al. (2018), it is not immediately clear how this would play a role in producing such a big difference with the C.C. in the plage region of our work. One possibility is that the visual criteria employed for the definition of plage in Bastian et al. (2018) allowed the inclusion of low T_{rad} and T_b areas in plage (for instance see lower plage mask in Figure 1f of Bastian et al. (2017), which clearly shows lower intensities for the majority of the pixels therein). In addition, the same study reported a C.C. of 0.80 between Mg II h to *ALMA*/Band6 T_b for the entire common FOV, which is not surprising given the overall similarity over a diverse set of features within that FOV, such as plage, sunspot umbra, and penumbra which appear morphologically similar. That is, a feature that is darker than the average intensity in the entire FOV in Mg II h, e.g., sunspot umbra, also appears dark in *ALMA*/Band6 and equivalently for plage regions (compare Figure 1a and 1c therein). This suggests that the mixing of regions with low T_{rad} and T_b in the brighter regions extracted as plage study may effectively increase the C.C.. Our expectation is supported after comparing the correlation matrix for the full FOV (mixed) with that for plage in Figure 10. The mixed correlation matrix treats all points of plage and periphery as one population (excluding the pore). While the C.C. for *ALMA*/Band6 T_b with Mg II k T_{rad} is 0.56 for plage and 0.57 for the periphery, the calculation for the full FOV increases the value dramatically, to a C.C. of 0.74, which amounts to 90% of the value reported in Bastian et al. (2018). The total number of pixels in the plage mask is 650 which becomes a final 578 pixels after the exclusion of the pore region (recall that we performed binning of 4 pixels along the y-direction). The total number of points in the periphery is 480. Thus, the inclusion of an additional 80% of plage periphery pixels (with about 2/3 showing low intensities) in the plage area made such a big difference in the C.C. for *ALMA*/Band6 T_b with Mg II k. While we cannot exclude the possibility of additional factors behind this discrepancy, e.g., different calibration methods employed in Bastian et al. (2018) and that the pixels in *IRIS* and *ALMA* observations were not selected on the basis of minimal time-difference constraints, it is possible that the inclusion of quieter-than-plage pixels,

like those in the periphery of plage here, play a significant if not a primary role in increasing the C.C. from a marginal value suggestive of intrinsic scatter between the observables to a value suggestive of a very high positive correlation (i.e., 0.80).

Jafarzadeh et al. (2019) focused on *ALMA*/Band6 and *IRIS* observations of the same region studied in Bastian et al. (2018), with an emphasis to extend the latter work by investigating relationships between T_b from *ALMA*/Band6 and T_{rad} from *IRIS* Mg II k and h (all line components), C II, and intensities of the optically thin Si IV and O I. However, Jafarzadeh et al. (2019) did not explore the C.C. from all combinations between the different observables as we do here (i.e., correlation matrices in Figure 10). Their region of plage was defined with a more quantitative measure than Bastian et al. (2018), i.e., as a region with photospheric magnetic fields $\geq \pm 0.2$ kG, a threshold value not too different from the one we use here. Indeed our magnetic map does not change if we use either ± 0.1 kG or ± 0.2 kG for thresholds. However, we note that their methodology lead to the inclusion of areas in the sunspot penumbra/superpenumbra that in Bastian et al. (2018) were excluded from their plage areas. Nevertheless, the region designated as plage in Jafarzadeh et al. (2019) above that superpenumbra/penumbra comprises the vast majority of the plage pixels in that work. To this we add that the regions of plage used in Bastian et al. (2018) are only partially within the FOV in Jafarzadeh et al. (2019) (i.e., further reducing the similarity of plage regions selected for the statistical studies of these two works). All these render the fair comparison with Bastian et al. (2018) even more problematic. To keep this subsection focused we moved some relevant (but important) details in the APPENDIX.

Contrary to Bastian et al. (2018) who calculated the C.C. between *ALMA*/Band6 T_b and the mean T_{rad} from Mg II h2v and h2r, the C.C. values in Jafarzadeh et al. (2019) were calculated separately for each individual line feature of Mg II T_{rad} with *ALMA*/Band6 T_b ; namely: for *ALMA*/Band6 T_b vs. T_{rad} Mg II k2v (and k2r) the C.C. was 0.73 (and 0.80), and 0.68 (0.78) for Mg II h2v (h2r). We found that the C.C. with our wavelength-integrated Mg II k T_{rad} was consistently higher than any of the other T_{rad} from individual Mg II k or h line features (by a few percent). Comparatively, the *ALMA*/Band6 with Mg II k2v (and k2r) was 48% (and 49%) higher than those calculated from our dataset of plage with line fitting; as for the Mg II h2v (h2r), that was 39% (42%) higher than our values respectively. Reconciling all the differences we mentioned between the work of Jafarzadeh et al. (2019) and our study but also the fact that both studies consider pixels with the least time-difference possible, the discrepancies between our scatterplots and theirs can be accounted for when features that are usually associated with pores or superpenumbra are included in the sample. If we do the same experiment as we did earlier in our comparison to Bastian et al. (2018) and include the periphery in our calculations, then the C.C. reported in Jafarzadeh et al. (2019) for Mg II k2v (and k2r) is only 7% (and 14%) higher than those calculated from our dataset; and for the Mg II h2v (and h2r), that is only 2% (and 11%) higher than ours, respectively. However, this experiment is more than suggestive for the discrepancy between our

work and Jafarzadeh et al. (2019): in Figure 3 and Figure 5e of Jafarzadeh et al. (2019) the *ALMA* and *IRIS* maps and the map showing the mask used for plage is provided. By also considering the time-difference map between the *ALMA* and *IRIS* pixels shown in Figure 4f therein, we can identify exactly which parts of the plage were used in the scatter plots of Figure 13 therein. There appear to be several locations with radial dark “lanes” or “streaks” of low T_{rad} and T_b around the superpenumbra/penumbra, and the majority of these pixels were used in the plage scatter plots of Jafarzadeh et al. (2019). Therefore, it is possible that the similarity of the results for plage reported by Jafarzadeh et al. (2019) and Bastian et al. (2018) and their discrepancy with our results may have the same origin: the difference in the criteria used in distinguishing regions of plage from other regions on the Sun.

Note that during the full time range of co-observations with *ALMA*/Band6, significant evolution was developing over the entire FOV. To get a clearer picture and to assess the similarities by considering the dynamic evolution in the common FOV, we further focus this analysis on Si IV and Mg II, which, thanks to the higher photon counts, permit the exploration of correlations with *ALMA*/Band6 at each time-step of our comprehensive dataset.

4.2.2. Time-Dependent Quantitative Study of Morphological Similarities Between Observables

In order to determine which regions in the common *ALMA-IRIS* FOV exhibit high morphological similarities between our set of observables, we split the FOV in sub-regions, or “correlation bins”, and we measure the C.C. between the different observables at each time step of our series. In the top panels of Figure 11 we show the size of the correlation bins on time-averaged, wavelength-integrated maps degraded with the *ALMA*/Band6 beam and position angle. Furthermore, we distinguish the sign of the C.C. – positive C.C., denoting positive correlation of the intensities, and negative C.C., representing anti-correlation. The latter will allow us to locate when and where such anti-correlation between (1) Mg II k, and (2) either Si IV or *ALMA*/Band6 occurs. The time-evolution of the C.C. per bin is presented in the form of time-plots in the bottom panels in Figure 11. For reference, we also show time-plots of the average time-evolution within the correlation bins for each of the observables as average intensity per bin. Note that for the calculation of the C.C. per bin per time-step we did not perform spatial averaging and we used all the individual pixels within each correlation bin at each time step. Also note that we have degraded the *IRIS* observables with the *ALMA*/Band6 beam size and position angle.

The resulting time-plots in Figure 11 vividly highlight the similarities and the differences between the observables. Again, as before, the raster series is integrated along wavelength centered on each line’s rest wavelength. Remarkably, the FOV of Mg II k and Si IV is split in locations of positive correlation and anti-correlation, confirming our initial visual determination of some locations of anti-correlation between these two observables (e.g., Figure 3; boxed regions in rasters). In addition, at times, there are certain locations where there is strong correlation between the intensities of Mg II k and Si IV, particu-

larly in the region containing the periphery of plage with the linear-like structures and the Type-II spicule. However, the most remarkable finding is the sporadic correlation (both in terms of intensity and time persistence) of *ALMA*/Band6 with Mg II k and the very high and more persistent correlation between *ALMA*/Band6 with Si IV across the entire FOV, with only a few instances of anti-correlation. Mg II k is found in anti-correlation with *ALMA*/Band6 in several locations in the FOV. The strong correlation between *ALMA*/Band6 and Si IV suggests that the spatial extent of bright features – as projected on the plane of the sky – is similar between these two observables, supporting that the geometric height of line formation of *ALMA*/Band6 and Si IV is similar.

Conversely, Mg II k and *ALMA*/Band6, even though they are nominally expected to have similar plasma temperature sensitivity, appear to sample different geometric heights in the solar chromosphere. This finding is consistent with the synthetic data from the model (Figures 6 and 7). Previous works (e.g., Bastian et al. 2017) considered that *ALMA*/Band6 forms at the mid-range of Mg II formation heights, but as we show later (§ 4.2.3) this does not appear to be the case. This is also supported by our study on time-averaged observables in the previous subsection § 4.2.1.2. Note, however, that we use wavelength-averaged rasters, and by averaging in wavelength the diagnostic information regarding the formation height of the Mg II k line is biased to lower heights as only Mg II k3 forms at the top of the chromosphere. In fact, in the Mg II k $x - t$ plot for $\tau = 1$ of Figure 6f for the maximum geometric height, we find a good match with geometric heights for *ALMA*/Band6 $\tau = 1$. However, Mg II k3 forms due to absorption – and thus, rasters in k3 are capturing the maximum absorption in that line. It is therefore our expectation that when Si IV and *ALMA*/Band6 show emission in dynamic plage structures (or spicules), Mg II k3 (which would be closer to *ALMA*/Band6 heights) has low intensity due to enhanced absorption. This can lead to anti-correlation with the other observables. We address this in the next section § 4.2.3.

For reasons of completeness, we perform this analysis on the synthetic observables produced from our model. In this case, since the simulation is 2.5D, the synthetic observables can be likened to a “sit-and-stare” *IRIS* observation, capturing the evolution across a “static 1D slit”. In Figure 12 we show the results. In the top panels we show how we split the domain in correlation bins (here, the bins are essentially 1D, arranged along the simulation domain’s x -direction at each time-step). As in the previous sections, the data have been degraded from the simulation’s scale size, $14 \text{ km (grid point)}^{-1}$, via gaussian convolution to adopt the nominal spatial resolution of *IRIS* rasters ($0'.16 \text{ pix}^{-1}$ along y -direction) and *ALMA* (degraded with the Band6 maximum beam size of $0'.8$). Then we further degrade the synthetic *IRIS* data by convolving the *ALMA*/Band6 beam size. In addition, we have masked out the location of emerging flux, which effectively separates the “spicules” region at the top of the FOV from the “plage” region at the bottom. The photospheric B_z shows significantly higher magnetic field strength for the plage region as compared to that in other locations of the domain (i.e., of order $\approx 100 \text{ G}$). Since we used the same “correlation bin” width with the

observations in Figure 11, only a few bins cover the domain in these time-plots. However, qualitatively, we get the same picture as before.

In Figure 12 we highlight the region of spicules with a solid ellipse and we use a dotted ellipse for the plage. For Mg II k and Si IV we see primarily anti-correlation for the plage region (compare PC1 dashed ellipse with solid PA1) and an alternation of correlation and anti-correlation for the spicule region (compare solid ellipses SC1 and SA1). The latter seems consistent with Figure 11 where the plage region in Mg II k and Si IV was more anti-correlated and showed a more intermixed correlation/anti-correlation for the plage periphery/spicule region (i.e., the anti-correlation plot in the observations shows less strong anti-correlation as compared to the plage regions north and south of the raster’s FOV). For *ALMA*/Band6 and Si IV we primarily see strong correlation for the plage (Figure 12; compare dotted ellipse PC2 with PA2), and some alternation between correlation and anti-correlation (with clear correlation during the time of the network jet, after $t=3,600 \text{ s}$) for the spicule region (compare area of solid ellipses SC2 with SA2). Last, for Mg II k and *ALMA*/Band6, we see anti-correlation for the plage region (compare PA3 with PC3), but a somewhat sporadic occurrence of correlation for the plage periphery/spicule region (compare area in solid ellipses SC3 with SA3; also positive correlation during the time of the network jet) intermixed in areas of anti-correlation, again in general agreement with previous comparison between *ALMA*/Band6 and *IRIS* observations (Figure 11).

4.2.3. Explaining the Morphological Similarities in the Synthetic Observables

In order to understand this interesting correlation in the observations we explore the time evolution in the emission and formation height of the synthetic observables for the region with spicules and plage (Figures 13 and 14, respectively). For our discussion, we select three representative time-steps along the evolution of spicules in the simulation. In addition, we select three wavelength positions for Si IV and Mg II k (taken in velocity space at $-13, 0$ and $+13 \text{ km s}^{-1}$ from the line cores). By doing so, we capture the wavelength dependence of the formation height of Si IV and Mg II k during the ascending and the descending phase of the spicule’s evolution in the space-time plots of Figure 8. At each time shown in Figures 13 and 14 we provide a wavelength-space plot (hereafter, “ $\lambda - x$ ”) for Mg II k (i.e., full spectral profile along the different positions in the simulation domain), which add relevant information in support of our interpretation presented in this subsection. An important result is that the synthetic Mg II k observable from the model shows a wide and well-defined k3 core. Studies on Mg II k synthesis from previous models had non-existent (or, at best, weak) k3 absorption due to the low densities in the upper-chromosphere for a combination of reasons, e.g., due to the absence of Type-II spicules (which can provide mass to greater geometric heights), and/or due to the lack of sufficient electron density, which in our model is now enhanced owing to the slow recombination rates in those heights (for an example of weak Mg II k3 absorption compare our results with Martínez-Sykora et al. 2017).

At the ascending phase of spicule 1 ($t=3,350$ s in Figure 13, position $x = [42, 44]$ Mm; spicule 2 has not started forming yet) we get emissivity in Si IV delineating the spicular column at the blue wing (-13 km s^{-1} ; panel a; dark green-to-white color outlining spicule 1), which closely corresponds to the height of *ALMA*/Band6 emission (shown with dark-red-to-white color in all panels). At the same time, in the area where spicule 2 would eventually develop (position $x = [40, 42]$ Mm) we can see significant Mg II k intensity in the blue wing (plotted at $\tau = 1$) (Figure 13a). In Figure 13d we show the $\lambda - x$ plot for this time with the Mg II k spectrum at each x -position of the domain, with clear RBE-signatures in the location of formation of spicule 2. Also, in the blue wing of Si IV (Figure 13a) we see a front at the tip of the structure delineated by Mg II k intensity (heights around $z=2.7$ Mm). This is consistent with the effects of a traveling shock waves in the chromosphere before the full development of a spicule (as the RBE signature suggests in Figure 4).

At the intermediate time-step shown in Figure 13 ($t=3,580$ s; middle column), spicule 2 has been fully developed and has almost reached its maximum elongation ($z=5$ Mm from the photosphere); most of Si IV emissivity now comes at the rest wavelength of the line (panel f; dark green-to-white color outlining spicule 2). Similarly, at the time of maximum elongation, *ALMA*/Band6 emission delineates the body of spicule 2 (note the close matching of geometric heights of line formation between *ALMA*/Band6 and Si IV; dashed ovals along spicule 2). The spectral profile of the optically thick Mg II (Figure 13h) shows that the k3 (“dark lanes” in the $\lambda - x$ plot highlighted with white dotted lines) has shifted at different wavelength positions across the spicule (e.g., panels f and g), and the respective geometric height of $\tau = 1$ at those different wavelength positions delineates different parts of the spicule (see dashed ovals in panels f and g). In fact, the spicule in Mg II appears as a dark feature (as compared to other locations in the domain), since the line is in absorption. This is due to the increased opacity or lower source function owing to the non equilibrium ionization effects.

In the last time-step shown here ($t=3,620$ s), spicule 2 has already begun to recede and the occurrence of the network jet brightening along the spicule strongly enhances the emission in Si IV at the core and in the red wing (panels j and k). The impulsive heating of the plasma in the spicule is so intense that forces *ALMA*/Band6 emission to come from lower heights where the plasma is cool enough (the spicule’s height seen in *ALMA*/Band6 effectively drops from $z\approx 5$ Mm to $z\approx 3$ Mm; shown with arrows in panels j). At the same time, while significant intensity in Mg II k emanates from low geometric heights (dashed ovals between $z=1 - 1.5$ Mm; panels i,j) at the blue wing and at line core, the Mg II k $\tau = 1$ height in the red wing (panel k) is much greater. There, we can see that Mg II k $\tau = 1$ roughly traces the length of the spicule, albeit in low intensity as compared to other locations with lower geometric heights (note that the same intensity range is used for each of the panels). This, again, is a manifestation of increased absorption. We point here to the anti-correlations seen in the $x - t$ plots between Si IV and Mg II k in the obser-

vations at the time of the network jet, where the Mg II k $x - t$ plot showed a “intensity depression” across different wavelength positions (Figure 5, location shown with dotted circle), even though there was a clear RBE signature at $\pm 55 \text{ km s}^{-1}$ (Figures 5 and 8). Here, Figure 13 (panel l) reproduces this behavior during the time of the network jet (pointed by an arrow in that panel).

The simulation captures clearly that the high correlation between spatially-resolved structures seen in *ALMA*/Band6 and Si IV is primarily due to the fact that the respective emissions emerge from similar parts of the same structure, both largely delineating the spicular column. Therefore, when observed at the plane of the sky (looking from the top of the simulation domain in this case, or, in other similar LOS, e.g., off the vertical) the spicule would manifest in both said observables and the high-intensity features would show up largely as spatially correlated. We cannot say the same, however, for Mg II k, as the $\tau = 1$ geometric height varies at different wavelength positions. However, we note a characteristic trend: during the ascending (descending) phase of the spicule, the $\tau = 1$ height at the blue (red) wing roughly delineates the spicule, albeit as a dark structure. There is also the following possibility: if the viewing angle (LOS) was tilted, say by 30° off the vertical towards small x (left side of the domain shown in Figure 13j,k), we would be seeing this effect to develop as: (i) bright Si IV; (ii) bright *ALMA*/Band6; and (iii) dark Mg II k, since the high intensity in Mg II k would be at the root of the spicule and the emission of (i) and (ii) would be projected against an area of low Mg II k background emission (e.g., for $x > 44$ Mm). This example illustrates one of the possible reasons that at certain locations in the observations Mg II intensity is anti-correlated to both Si IV and *ALMA*/Band6.

The relationship between the ascending/descending phase of mass motions with Doppler shift and emissivity in Si IV is also seen in the plage region of the simulation (Figure 14). At $t=3,400$ s a dynamic fibril shoots mass upwards ($x = [27, 29]$ Mm), where in the blue wing a “front” of Si IV emissivity is closely followed by emission in *ALMA*/Band6 (panel a; dashed oval). Mg II k intensity comes from greater geometric heights but in absorption, again, in contrast to other locations in the domain, which are brighter but at much lower geometric heights ($z\approx 0.5-1$ Mm). Similarly, relatively low intensity is seen at the nominal rest wavelength of Mg II k (panel b). This, again, pinpoints the reasons behind the anti-correlation we noted between Mg II k and the well-correlated pair of *ALMA*/Band6 and Si IV, both in the simulation and the observations of plage. Moving forward at the times of the other two time-steps ($t=3,510$ s and $3,580$ s), we see a consistent evolutionary pattern between *ALMA*/Band6 and Si IV. That is, when the bulk of the mass in the dynamic fibril stalls, we get emission from Si IV line-core (panel f) and when the mass is receding back to the surface, Si IV emits in the red wing, again, closely followed by *ALMA*/Band6 emission (panel k). We also note that at those times high intensity in Mg II k comes primarily from lower heights in the atmosphere (see panels i, j, and dashed oval in panel k).

Therefore, we conclude that *ALMA* is sensitive to the cool-to-warm plasma existing at the highest parts of ei-

ther spicules and dynamic fibrils but just below their tips. These locations are subject to shocks or other cooling/heating mechanisms (such as ambipolar heating or cooling by adiabatic expansion), which may raise the plasma to high temperatures, eventually causing it to emit in Si IV ($T \approx 80,000$ K) or even lower temperatures. Subsequently, the temperature drops down to a level that *ALMA*/Band6 is sensitive to (8,000-10,000 K), in geometric heights not far from those of transition region temperatures. This finding gives insights on the multi-thermal nature of spicules (Chintzoglou et al. 2018). All the above result in the high similarity between Si IV and *ALMA*/Band6 seen in the observations. With regards to Mg II k, depending on the viewing angle and on how clearly such effects are seen against the background, comparisons with the other observables may show a loss of correlation, or, if there is regularity in the appearance and positioning of such structures within the FOV, anti-correlation may also arise (i.e., bright features in one observable/pass band “complementing” dark structures in another). This seems to be reasonable when spicules or dynamic fibrils are bright in Si IV and *ALMA*/Band6 but manifest as low intensity features in Mg II (due to enhanced absorption and/or due to low intensity in comparison to Mg II k intensities from other locations; for the case of dynamic fibrils this may be related to similar effects that were seen in space-time plots of bright grains in the work of Skogsrud et al. 2016).

4.3. Measuring the Temperature Increase in the Aftermath of Shocks Above Plage

Apart from the identified Type-II spicule, the common *IRIS* and *ALMA*/Band6 FOV also contains part of a strong magnetic field plage region that is very dynamic. In this subsection we focus on the dynamics seen in the plage region and we explore the potential of *ALMA*/Band6 observations in measuring the plasma temperature and its time evolution in regions dominated by the passage of chromospheric shocks.

Here, with *IRIS* observing in Mg II k and Si IV we can see the chromospheric shocks as they propagate higher in the chromosphere/transition region. Focusing on the north part of the common *IRIS* and *ALMA*/Band6 FOV we see a lot of recurrent activity as brightenings above the plage, and also some plane-of-the-sky motions of bright dynamic fibrils. Chromospheric plage exhibits features known as dynamic fibrils, driven by slow-mode magnetoacoustic shocks which pervade the plage region (Hansteen et al. 2006; De Pontieu et al. 2007a; Langanen et al. 2008). From our 34 min-long time series we calculate the autocorrelation at each pixel in the Mg II FOV to determine locations of activity segmented by the characteristic lifetimes of the signal, such as intensity modulations caused by chromospheric shocks. da Silva Santos et al. (2020) have reported a periodicity for shocks in Mg II k of 3.5 to 4 min in plage. In the areas above plage at Mg II k2v we found autocorrelation times of ≈ 150 -200 s but also some even “slower” locations of ≈ 300 s. Using this autocorrelation map as a guide we select a $1'' \times 1''$ sub-region (corresponding to a 3×6 pixels for *IRIS* rasters and 6×6 pixels for *ALMA*/Band6) that is well within plage (position $(x, y) = (4, 17)''$ in the raster FOV of Figure 3) in order to explore if *ALMA* can be used to study chromospheric shocks. Within the selected

region, we produce λ -t plots for Si II and Mg II k *IRIS* rasters and extract the T_b from *ALMA*/Band6. Furthermore, to improve the contrast in the λ -t plots we filter them with an unsharp-mask image processing operation with a 5-pixel radius. Also, to enhance weak features that were still not visible in the wings of the lines, we produced the time-derivative of the direct λ -t maps. We present the results in Figure 15.

As a shock passes through the chromosphere above plage, a typical behavior is seen in λ -t plots of chromospheric lines: a blue-shifted excursion slowly drifts toward the red wing of the line, until a new blue-shifted excursion appears again, and so on, producing a “sawtooth” pattern in the λ -t plot. This “sawtooth” pattern is seen in Mg II k λ -t with sudden increases of the intensity in the far blue wing that sweep through the dark k3 core and then reach the red wing typically with a new enhancement in the blue wing (Figure 15b; see enhancements above yellow line in the blue wing). Similarly, blue-shifted enhancements appear in Si IV (Skogsrud et al. 2016) in tandem with the excursions in Mg II k (Figure 15bd). We overplot the *ALMA*/Band6 T_b over the λ -t plots for the same selected region above plage. Despite the data gaps in *ALMA*/Band6 observations, the behavior of T_b jumps is strikingly similar to the wavelength-drift trends due to the passage of the shocks in the chromosphere. In Figure 15ac we enhance the signatures of the onsets of shocks in the time-derivative plots and mark them with arrows. In fact, when looking at the blue wing, the similarity of the λ -t time evolution with *ALMA*/Band6 is more obvious for Si IV than for Mg II k (see prominent blueshifts in Si IV λ -t plot in areas pointed by arrows 2,3,4,5 in panel d), which may have to do with the similarity of *ALMA*/Band6 mm-emission formation height with Si IV we determined in the present paper. This result may also be consistent with da Silva Santos et al. (2020) who through inversions determined that during the passage of shocks the *ALMA*/Band6 emission appears to emerge from lower optical depths.

Our interpretation is that the *ALMA*/Band6 observations in plage are sensitive to the localized heating of the upper chromosphere/lower transition region, produced by the passage of shocks. The jumps in T_b are of order 10%-20% increase from a baseline value of $\approx 7,500$ K (maximum jump at 8,500 K). The observed decay time down to the baseline value is of order ≈ 60 -120 s. However, note that for Si IV λ -t the signal in the selected pixel position in the raster occasionally becomes poor due to low photon counts in the FUV range of the *IRIS* spectrograph. The 3×6 pixels for *IRIS* seems to improve the signal. We also note that the bright signatures of shocks seen in the rasters are not confined to one pixel location and appear to move in the plane of the sky until they fade. Again, the 3×6 pixel window compensates for the most part of the plane-of-the-sky motions seen in the movie. There are times when the recurrence of brightenings took place every ≈ 120 s (at least in the early phase of the plots; see arrows 1, 2 and 3 in panel b). This may suggest that a given location above plage may be pervaded by shocks coming from different directions which arrive at comparable timings. Such occasions may cause the periodicity patterns to modulate with shorter or even irregular periods. In addition, note

that the spatial resolution of *ALMA*/Band6 maps is significantly worse as compared to that of the *IRIS* rasters (by approximately one order of magnitude), thus the filling factor of the shock (at the *ALMA*/Band6 beam size) is less than 1 (as compared to the spatial scales resolved with *IRIS*). Therefore, even though such 1000 K-jumps in mm-emission appear consistent with heating due to shocks suggested by Wedemeyer-Böhm et al. (2007), we conclude that the true temperature enhancements may be even higher locally. Nevertheless, our work presents indications for the localized heating of the chromospheric plasma in plage regions by shocks that travel through the geometric height of formation of *ALMA*/Band6 free-free emission.

5. SUMMARY & CONCLUSIONS

In this work we focused on addressing the nature and the dynamics of chromospheric/transition region structures found in plage, namely, fibrils, jet-like features (Type-II spicules) and traveling shocks using high time-cadence and high spatial resolution data from the *ALMA* and *IRIS* observatories. Our target was a plage region in the leading part of NOAA AR 12651. The spatial distribution of the plage region in the FOV allowed the simultaneous observation of regions of high chromospheric emission in addition to regions with low background emission; the former allowed the study of chromospheric shocks and the latter permitted the first unambiguous on-disk observation of a spicule with *ALMA*/Band6 observations. Thanks to this favorable observing geometry, our analysis was free from difficulties faced in previous works, such as low signal-to-noise ratio and strong LOS superposition in the data, which is common in observations of spicules at the limb. In addition, to assist the interpretation of these unique observations, we employed a 2.5D numerical simulation (Bifrost model) of spicules considering ambipolar diffusion in non-equilibrium ionization conditions. We produced synthetic observables to compare the model with our observations from *ALMA*/Band6 and *IRIS*. Last, we performed a first-cut study on the heating of the chromosphere above plage by measuring the brightness temperature modulation due to passing shocks with *ALMA*/Band6.

Our main findings can be summarized as follows:

1. We conclude that the dynamic linear structure captured in the common *IRIS* and *ALMA*/Band6 FOV is a Type-II spicule. This is supported by (a) the slender profile of the structure, (b) the Rapid Blueshifted Excursion (RBE) in the spectrum of Mg II k and Si IV from the bulk of the structure (Figure 4), (c) the dynamics seen in the space-time plot (parabolic space-time profile; Figure 5) in the observations and in the space-time plots from synthetic observables produced from the simulation (Figure 6).
2. The identified spicule experienced a network jet brightening (apparent speed $\approx 95 \text{ km s}^{-1}$). Our synthetic observables (Figure 8) compared with the observations (Figures 5 and 9) show a clear agreement with each other, including the occurrence of a network jet brightening in the simulation (apparent speed $\approx 140 \text{ km s}^{-1}$). Note that the *IRIS*

raster time-cadence was at 26 s (while the simulation's time-cadence was at 10 s), each posing a lower limit in the deduced apparent speed. This apparent brightening in Si IV likely occurred due to a rapidly-propagating heating front along the spicular mass, instead of representing rapid upward mass flows (consistent with De Pontieu et al. 2017b; Chintzoglou et al. 2018). In fact, both the observed and the simulated spectra show a clear red-blue asymmetry suggesting mass motions directed away from the observer during the time of the network jet.

3. We confirm the multi-thermal nature of dynamic Type-II spicules (Chintzoglou et al. 2018). The tricolor space-time plot (combining *ALMA* and *IRIS* observables; Figure 9) reveals a picture strongly suggesting that the spicular plasma emits in multiple temperatures simultaneously, also supported by synthetic observables from the Bifrost simulation (Figure 6).
4. We report a very high degree of similarity for features seen in plage between *ALMA*/Band6 and *IRIS*/SJI 1400 Å and Si IV 1393 Å rasters (Figure 3). By considering both the observations and the simulation (Figure 6) and by performing a rigorous study of the time-evolution of spatial correlations between different observables (Figure 11), we conclude that *ALMA*/Band6 is sensitive to the cool plasma at the highest parts of the spicules and dynamic fibrils (i.e., in plage), which is next (because of the locally large temperature gradients) to plasma that emits in Si IV ($T \approx 80,000 \text{ K}$, transition region temperatures).
5. We also noted an interesting anti-correlation between intensity features seen in Si IV and Mg II *IRIS* rasters (intensity depressions Mg II k highlighted in Figure 3) and in the resulting space-time plots (i.e., Mg II k intensity depression visible in the observations in Figure 5 and in the simulation in Figure 8). We conclude that the apparent anti-correlation or lack of correlation (which may in part be due to observing different parts of the same events/structures either as cospatial or even as non-cospatial owing to LOS projection effects) has its origin in Mg II opacity effects in plage structures. Strong absorption is the reason behind the low Mg II intensities emerging from greater geometric heights in the locations of spicules (Figure 13).
6. For plage we report a low linear C.C. (0.49 to 0.55) for *ALMA*/Band6 T_b with Mg II for any of the k2v/k2r/h2v/h2r line features and a maximum of 0.56 for wavelength-integrated Mg II k that contains all the k-line features (either as intensity maps in $[\text{DN s}^{-1}]$ or maps expressed as radiative temperatures in [K]). Our results are quantitatively in contrast with previous works (e.g., Bastian et al. 2018, and Jafarzadeh et al. 2019, since both of them focused on the same observations which reported higher C.C. values in plage). We also determined that by including quieter areas in the plage sample,

i.e., considering a mixed area of plage and periphery of plage as “plage”, it greatly increased the C.C. between *ALMA*/Band6 T_b with T_{rad} from Mg II k and h, producing values as high as those in Bastian et al. (2018) and Jafarzadeh et al. (2019). In fact, these two studies, despite their methodological differences, report similarly high C.C. values that may essentially be interpreted as independent confirmation of each other’s results. We thus caution on the different criteria employed for defining plage regions, which may lead to unwanted bias in quantitative studies between different observables.

7. The definition of the spatial extent of plage is not formally well-defined in the previous literature. Here, our empirical approach appears to separate better the surrounding regions from plage itself than previous approaches that, e.g., determined plage regions “by-eye” or via a “blind” use of masks from thresholded magnetogram or chromospheric intensity maps (§ 4.2.1.1). We also add that the C.C. is a very sensitive statistical measure. A small amount of outliers in a scatter plot can greatly affect the C.C. value. Thus given the high sensitivity of C.C. and its application in cases where plage cannot be robustly classified with conventional techniques (e.g. due to the presence of pores, or being too close to sunspot penumbras) we caution that the C.C. values between T_{rad} and T_b in plage can be actually lower, i.e., as low as those we report in the present paper.
8. It has been previously reported (Bastian et al. 2017; Jafarzadeh et al. 2019) that there is scatter between radiative temperatures from Mg II and brightness temperatures from *ALMA*/Band6, with a suggested cause of the scatter being the Mg II source function decoupling from the local conditions. Our work here demonstrates that the scatter is more significant than previously thought and highlights another reason behind its nature: both the observations (i.e., *ALMA*/Band6 is mostly similar with Si IV and not with Mg II) and the simulation suggest that the formation height for *ALMA*/Band6 emission is above that of Mg II for most wavelengths along the Mg II line, even though both Mg II and *ALMA*/Band6 are sensitive to a similar range of temperatures. This formation height difference can contribute to the large scatter. While our observational results are also supported by the simulation, for the latter we caution that the model was not simulating a specific spicule, thus differences may be between the simulation and the observed spicule (e.g., in the magnetic field strength and structure, the magnitude of electric currents, etc). We also caution that the model should not be taken as a perfect representation of the plage atmosphere. For example, the distribution of modeled brightness temperatures of *ALMA*/Band6 is lower by 2,000 K as compared to those in the observations.
9. We performed a thorough quantitative study on the similarities between time-averaged Si IV, C II

(wavelength-integrated intensities), Mg II k (average T_{rad}), and *ALMA*/Band6 (T_b) maps (Figure 10). We report that the highest C.C. is obtained between any combination of the triad of Si IV, C II and *ALMA*/Band6, the lowest C.C. is obtained between Mg II k - Si IV and Mg II k - *ALMA*/Band6. In addition, C II is found in moderate-to-high C.C. with all other observables. We conclude that this study provides evidence on the general tendency for the order of the formation heights of all these different observables with geometric height. That is, Mg II k (wavelength-integrated) intensity (T_{rad}) emerges from lower geometric heights in the plage atmosphere, with Si IV forming at the greatest heights (with a formation temperature $T \approx 80,000$ K, placing it in the transition region). The good agreement of C II with all observables is due to having, on average, a formation height between that of Mg II k and Si IV. This result seems consistent with the work of Rathore et al. (2015b) based on the analysis of a numerical simulation.

10. We present indications of heating by shocks propagating in the chromosphere with *ALMA*/Band6 (beam size $\approx 0''.7 \times 0''.8$). We found a repetitive increase-and-decrease of the local chromospheric plasma temperature above plage of order 10-20% from a basal value of 7,500 K (for comparison, the temperature for a location in the periphery of plage was found $\approx 5,500$ K), with a decay time back to the baseline of about 60-120 s (Figure 15). In simulations presented in Wedemeyer-Böhm et al. (2007) shocks manifest as enhancements in the mm continua of the order of 1000 K. da Silva Santos et al. (2020) had determined that the shock wave pattern in Mg II k was between 3.5 and 4 min ($\lesssim 5$ mHz). However, here, we also find signs of mixed signal with a recurrence at around 120 s. This may suggest that a specific location in plage may be pervaded by shocks coming from different directions and at different timings, making at times the periodicity patterns to appear as if they modulate with shorter or even irregular periods. da Silva Santos et al. (2020) performed inversions of *IRIS* with *ALMA* and reported that emission from shocks in the *ALMA*/Band6 plage appears as coming from lower optical depths (i.e., higher geometric heights) in comparison to that in weakly magnetized areas (e.g., in the plage periphery). This appears consistent with our determination of the formation height for *ALMA*/Band6, which seems to be just below that of Si IV as we show in the present paper.

This work demonstrates the benefits of the synergy between *ALMA* and *IRIS* observations, which effectively expanded the diagnostic potential of each observatory, and also tested and provided constrains for advanced numerical simulations.

This paper makes use of the following *ALMA* data: ADS/JAO.ALMA#2016.1.00050.S. *ALMA* is a partnership of ESO (representing its member states), NSF (USA) and NINS (Japan), together with NRC (Canada),

MOST and ASIAA (Taiwan), and KASI (Republic of Korea), in cooperation with the Republic of Chile. The Joint *ALMA* Observatory is operated by ESO, AUI/NRAO and NAOJ. We gratefully acknowledge support by NASA contract NNG09FA40C (IRIS). JMS is also supported by NASA grants NNX17AD33G, 80NSSC18K1285 and NSF grant AST1714955. JdlCR is supported by grants from the Swedish Research Council (2015-03994), the Swedish National Space Board (128/15) and the Swedish Civil Contingencies Agency (MSB). This project has received funding from the European Research Council (ERC) under the European Union's Horizon 2020 research and innovation programme (SUNMAG, grant agreement 759548). MS, SJ and SW are supported by the SolarALMA project, which has received funding from the European Research Council (ERC) under the European Unions Horizon 2020 re-

search and innovation programme (grant agreement No. 682462), and by the Research Council of Norway through its Centres of Excellence scheme, project number 262622. The simulations and Mg II synthesis were ran on clusters from the Notur project, and the Pleiades cluster through the computing project s1061, s1630, and s2053 from the High End Computing (HEC) division of NASA. This research is also supported by the Research Council of Norway through its Centres of Excellence scheme, project number 262622, and through grants of computing time from the Programme for Supercomputing. *IRIS* is a NASA small explorer mission developed and operated by LMSAL with mission operations executed at NASA Ames Research center and major contributions to down-link communications funded by ESA and the Norwegian Space Centre. HMI and AIA are instruments on board *SDO*, a mission for NASAs Living with a Star program.

REFERENCES

- Auer, L. 2003, *Astronomical Society of the Pacific Conference Series*, Vol. 288, *Insight into Multi-Dimensional Transfer*, ed. I. Hubeny, D. Mihalas, & K. Werner, 405
- Bastian, T. S., Chintzoglou, G., De Pontieu, B., et al. 2017, *ApJ*, 845, L19
- . 2018, *ApJ*, 860, L16
- Bose, S., Henriques, V. M. J., Joshi, J., & Rouppe van der Voort, L. 2019, *A&A*, 631, L5
- Carlsson, M., De Pontieu, B., & Hansteen, V. H. 2019, *ARA&A*, 57, 189
- Carlsson, M., Leenaarts, J., & De Pontieu, B. 2015, *ApJ*, 809, L30
- Carlsson, M., & Stein, R. F. 1997, *ApJ*, 481, 500
- . 2002, *ApJ*, 572, 626
- Chintzoglou, G., De Pontieu, B., Martínez-Sykora, J., et al. 2018, *ApJ*, 857, 73
- Cotton, W. D. 2017, *PASP*, 129, 094501
- da Silva Santos, J. M., de la Cruz Rodríguez, J., Leenaarts, J., et al. 2020, *A&A*, 634, A56
- de la Cruz Rodríguez, J. 2019, *A&A*, 631, A153
- de la Cruz Rodríguez, J., De Pontieu, B., Carlsson, M., & Rouppe van der Voort, L. H. M. 2013, *ApJ*, 764, L11
- de la Cruz Rodríguez, J., Leenaarts, J., & Asensio Ramos, A. 2016, *ApJ*, 830, L30
- De Pontieu, B., Hansteen, V. H., Rouppe van der Voort, L., van Noort, M., & Carlsson, M. 2007a, *ApJ*, 655, 624
- De Pontieu, B., Martínez-Sykora, J., & Chintzoglou, G. 2017b, *ApJ*, 849, L7
- De Pontieu, B., McIntosh, S. W., Hansteen, V. H., & Schrijver, C. J. 2009, *ApJ*, 701, L1
- De Pontieu, B., McIntosh, S. W., Carlsson, M., et al. 2007b, *Science*, 318, 1574
- De Pontieu, B., McIntosh, S. W., Carlsson, M., et al. 2011, *Science*, 331, 55
- De Pontieu, B., Title, A. M., Lemen, J. R., et al. 2014, *Sol. Phys.*, 289, 2733
- Golding, T. P., Leenaarts, J., & Carlsson, M. 2016, *ApJ*, 817, 125
- Gudiksen, B. V., Carlsson, M., Hansteen, V. H., et al. 2011, *A&A*, 531, A154
- Hansteen, V. H., De Pontieu, B., Rouppe van der Voort, L., van Noort, M., & Carlsson, M. 2006, *ApJ*, 647, L73
- Henriques, V. M. J., Kuridze, D., Mathioudakis, M., & Keenan, F. P. 2016, *ApJ*, 820, 124
- Iijima, H., & Yokoyama, T. 2017, *ApJ*, 848, 38
- Jafarzadeh, S., Wedemeyer, S., Szydlarski, M., et al. 2019, *A&A*, 622, A150
- Klimchuk, J. A. 2012, *Journal of Geophysical Research (Space Physics)*, 117, A12102
- Kurucz, R. L. 1970, *SAO Special Report*, 309
- Langangen, Ø., De Pontieu, B., Carlsson, M., et al. 2008, *ApJ*, 679, L167
- Leenaarts, J., Carlsson, M., Hansteen, V., & Rutten, R. J. 2007, *A&A*, 473, 625
- Lemen, J. R., Title, A. M., Akin, D. J., et al. 2011, *Sol. Phys.*, 115
- Loukitcheva, M., Solanki, S. K., Carlsson, M., & White, S. M. 2015, *A&A*, 575, A15
- Martínez-Sykora, J., De Pontieu, B., Carlsson, M., et al. 2017, *ApJ*, 847, 36
- Martínez-Sykora, J., De Pontieu, B., De Moortel, I., Hansteen, V. H., & Carlsson, M. 2018, *ApJ*, 860, 116
- Martínez-Sykora, J., Leenaarts, J., De Pontieu, B., et al. 2020, *ApJ*, 889, 95
- McMullin, J. P., Waters, B., Schiebel, D., Young, W., & Golap, K. 2007, *Astronomical Society of the Pacific Conference Series*, Vol. 376, *CASA Architecture and Applications*, ed. R. A. Shaw, F. Hill, & D. J. Bell, 127
- Nóbrega-Siverio, D., Martínez-Sykora, J., Moreno-Insertis, F., & Carlsson, M. 2020, arXiv e-prints, arXiv:2004.11927
- Patsourakos, S., Klimchuk, J. A., & Young, P. R. 2014, *ApJ*, 781, 58
- Pereira, T. M. D., & Uitenbroek, H. 2015, *A&A*, 574, A3
- Pereira, T. M. D., De Pontieu, B., Carlsson, M., et al. 2014, *ApJ*, 792, L15
- Pesnell, W. D., Thompson, B. J., & Chamberlin, P. C. 2012, *Sol. Phys.*, 275, 3
- Rathore, B., Carlsson, M., Leenaarts, J., & De Pontieu, B. 2015a, *ApJ*, 811, 81
- Rathore, B., Pereira, T. M. D., Carlsson, M., & De Pontieu, B. 2015b, *ApJ*, 814, 70
- Rau, U., & Cornwell, T. J. 2011, *A&A*, 532, A71
- Rouppe van der Voort, L., De Pontieu, B., Pereira, T. M. D., Carlsson, M., & Hansteen, V. 2015, *ApJ*, 799, L3
- Scherrer, P. H., Schou, J., Bush, R. I., et al. 2012, *Sol. Phys.*, 275, 207
- Schmit, D., Bryans, P., De Pontieu, B., et al. 2015, *ApJ*, 811, 127
- Secchi, A. 1877, *Le Soleil. Seconde partie. Structure du Soleil (suite) – Activite extérieure*, Gauthier Villars, Paris
- Shimojo, M., Bastian, T. S., Hales, A. S., et al. 2017, *Sol. Phys.*, 292, 87
- Shimojo, M., Kawate, T., Okamoto, T. J., et al. 2020, *ApJ*, 888, L28
- Skogsrud, H., Rouppe van der Voort, L., & De Pontieu, B. 2016, *ApJ*, 817, 124
- Tian, H., DeLuca, E. E., Cranmer, S. R., et al. 2014, *Science*, 346, 1255711
- Tripathi, D., & Klimchuk, J. A. 2013, *ApJ*, 779, 1
- Uitenbroek, H. 2001, *ApJ*, 557, 389
- Vourlidis, A., Beltran, S. T., Chintzoglou, G., et al. 2016, *Journal of Astronomical Instrumentation*, 5, 1640003
- Wedemeyer, S., Bastian, T., Brajša, R., et al. 2016, *Space Sci. Rev.*, 200, 1
- Wedemeyer, S., Szydlarski, M., Jafarzadeh, S., et al. 2020, *A&A*, 635, A71
- Wedemeyer-Böhm, S., Ludwig, H. G., Steffen, M., Leenaarts, J., & Freytag, B. 2007, *A&A*, 471, 977
- White, S. M., Iwai, K., Phillips, N. M., et al. 2017, *Sol. Phys.*, 292, 88

- Wooten, A., & Thompson, A. R. 2009, IEEE Proceedings, 97, 1463
- Yokoyama, T., Shimojo, M., Okamoto, T. J., & Iijima, H. 2018, ApJ, 863, 96

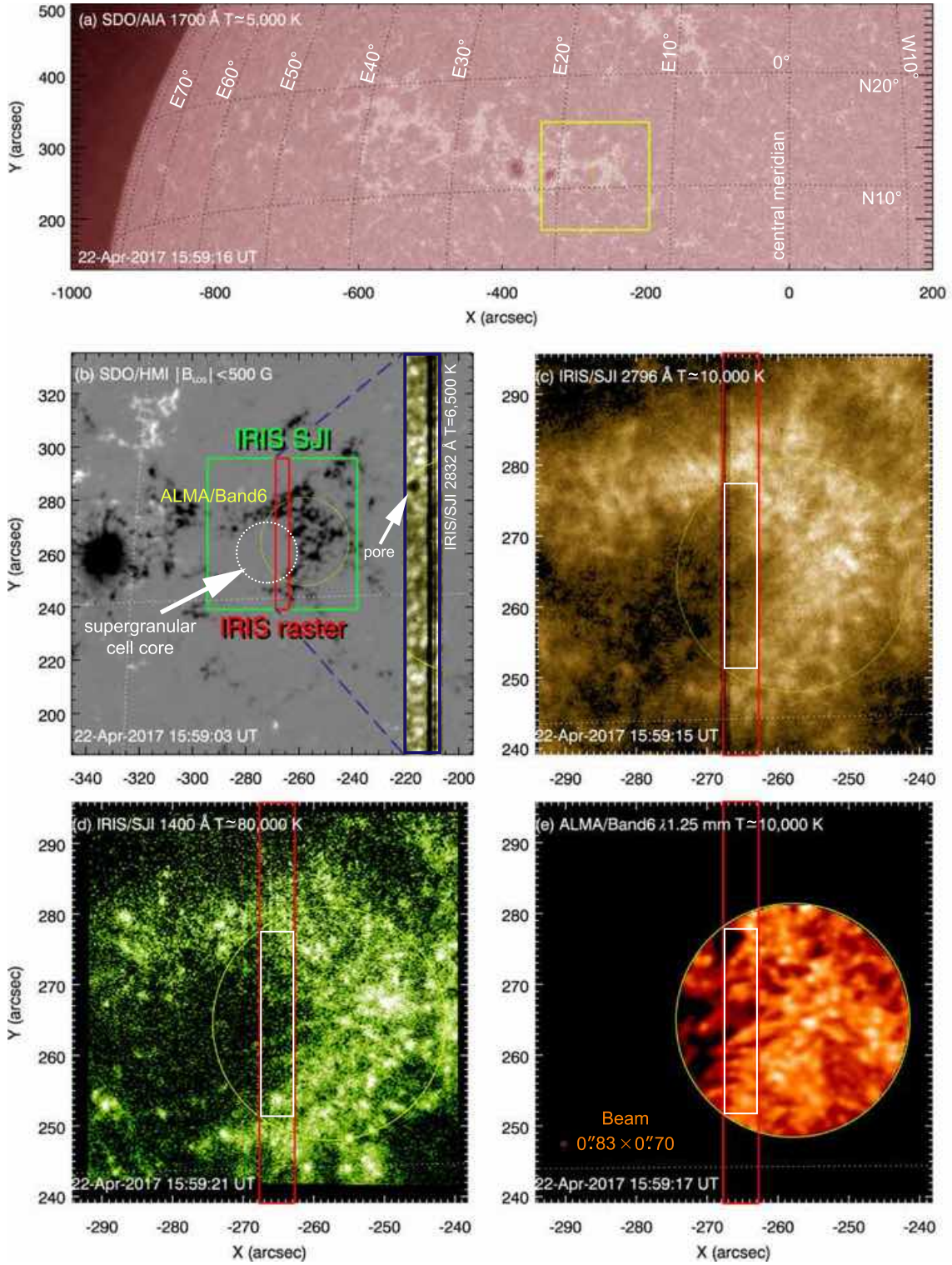


FIG. 1.— (a) Context figure from *SDO*/AIA 1700 Å showing the location of the plage region observed by *IRIS* and *ALMA*. (b) The magnetic field distribution from *SDO*/HMI is shown for the boxed area in panel (a). The same panel contains a narrow width inset plot of the *IRIS*/SJI 2832 Å (Mg II continuum). (c) Mg II 2796 Å and (d) Si IV 1400 Å corresponding to the *IRIS*/SJI FOV (green box) in panel (b). The corresponding *ALMA*/Band6 FOV is shown in panel (e). The white rectangle marks the FOV of the raster cutout shown in Figure 3 (i.e., trimmed along the y-direction to focus on the common *ALMA*/*IRIS* FOV).

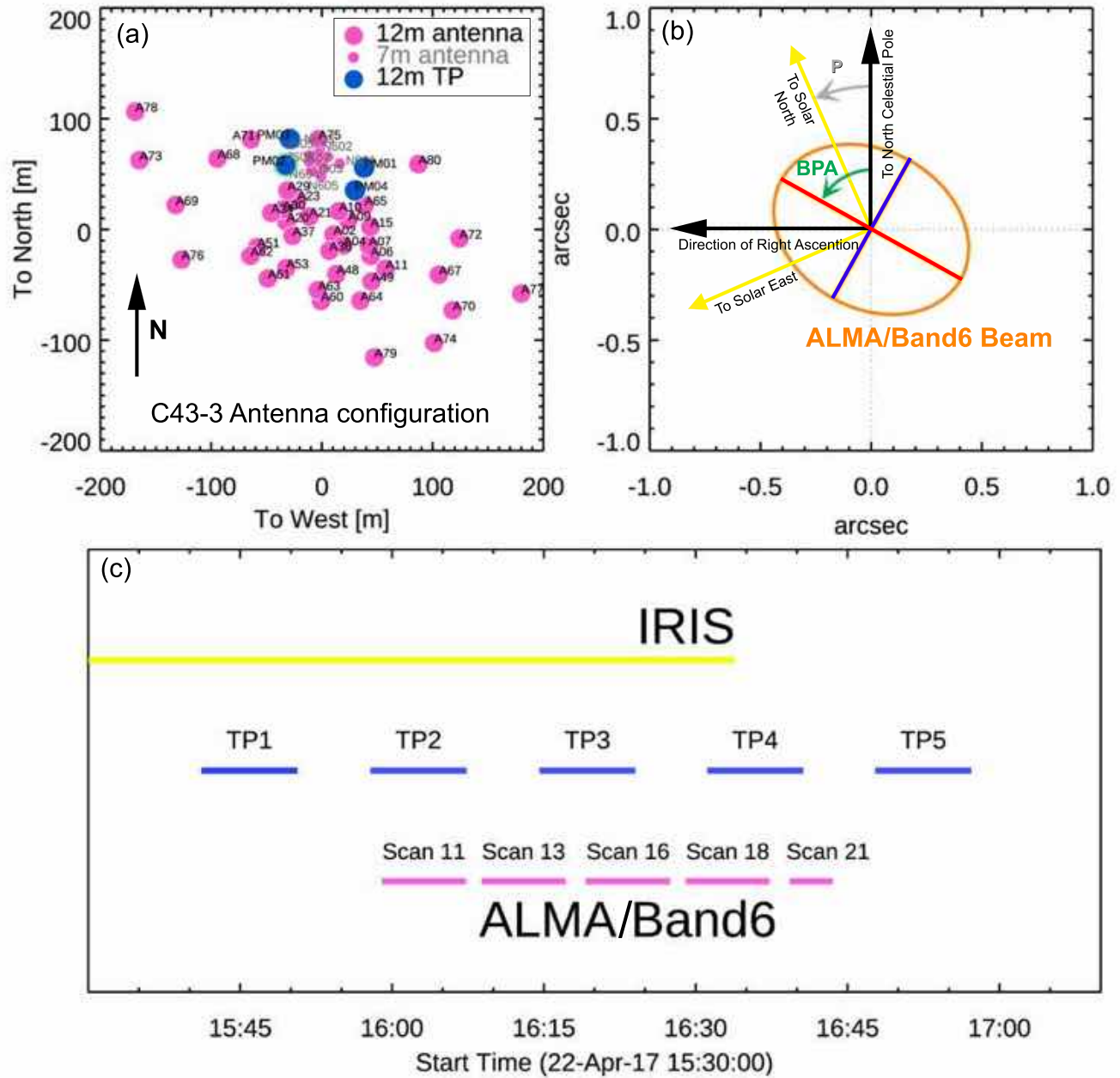


FIG. 2.— (a) *ALMA* antenna configuration at the time of the observations. Three out of forty-three 12 m-array antennas were excluded due to problems with their calibration; similarly, only nine antennas in the 7 m array were included. For the TP measurements only one 12 m TP antennas was used (highlighted with a green circle). The labels correspond the specific identification name of each antenna. (b) The resolution element in the interferometric imaging (i.e., the “beam”), is a 2D gaussian full-width at half-maximum with a major (red) and a minor (blue) axis. The beam’s position angle (BPA) is measured between the north celestial pole and the beam major axis counter-clock-wise, like the solar P angle. Note that the solar P angle at the time of the observations was negative, i.e., $\approx -25^\circ$. (c) Timeline of joint *ALMA*/Band6 and *IRIS* observations. Scans are interrupted by special scans (not shown) required for calibrations of the interferometric array.

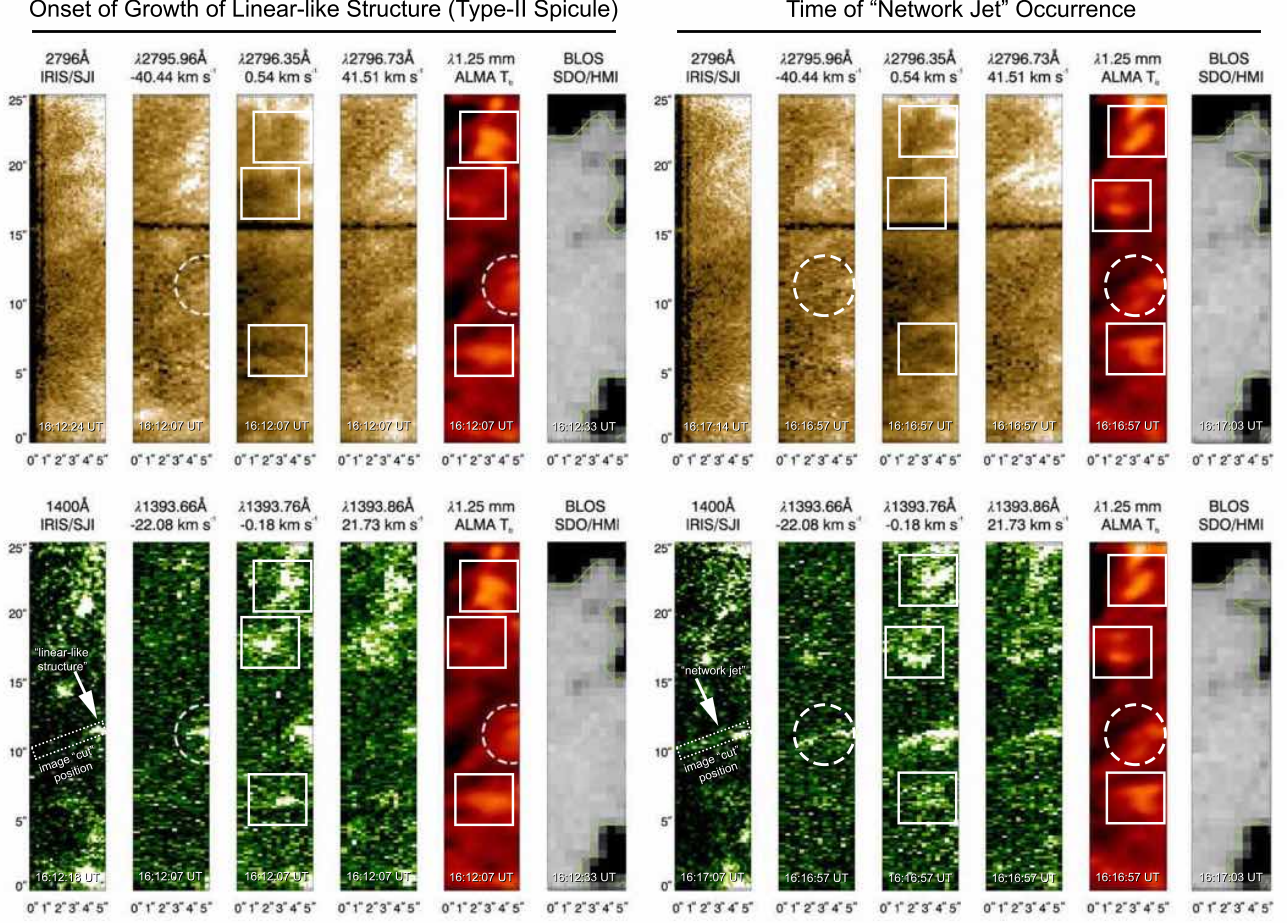


FIG. 3.— Inter-comparison of *IRIS* and *ALMA*/Band6 observations at two different times in the evolution of the linear-like structure. Raster scans are shown at selected wavelength positions in Mg II (top) and Si IV (bottom) showing the clear appearance of the rapidly evolving structure in Mg II and Si IV (dashed circles). Boxed areas denote locations where intensity features in the Mg II maps appear anti-correlated to those in Si IV and *ALMA*/Band6 maps. In the 1400 Å *IRIS*/SJI panels we show the position of the image cut we performed on each observable to produce Figure 5. In the panels with the *SDO*/HMI magnetograms (scaling clipped at ± 250 G) we overplot an isocontour of ± 100 G. The FOV is thus split into two strongly magnetized areas (north and south of the FOV) separated by a weakly magnetized area (in the middle).

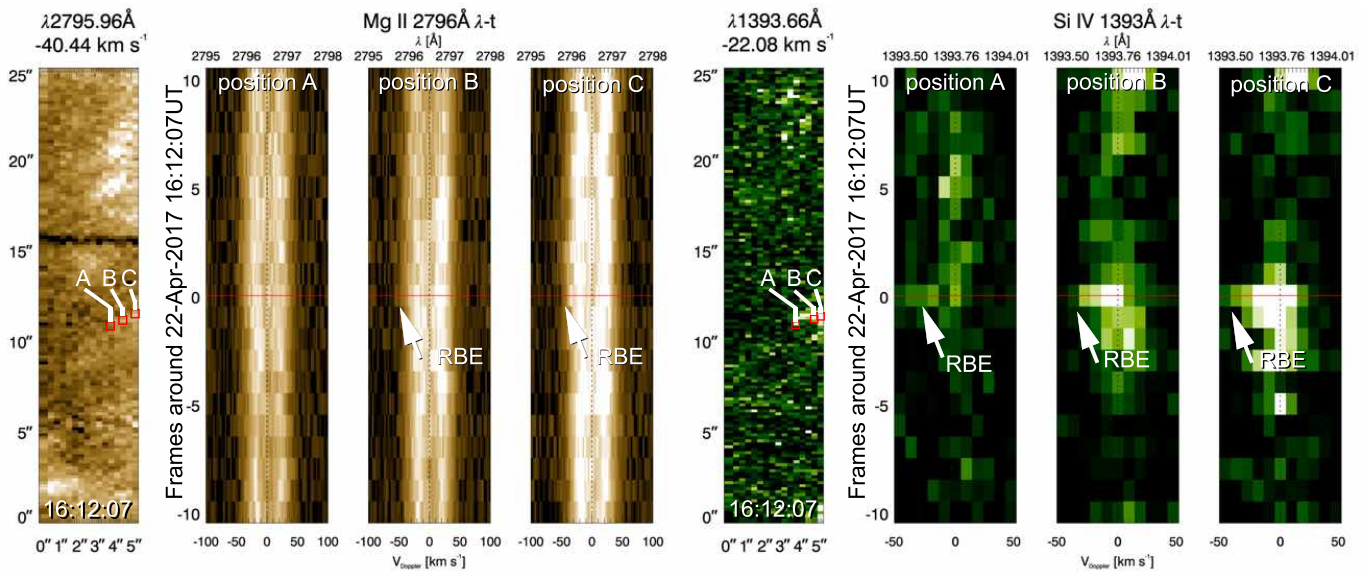


FIG. 4.— $\lambda-t$ plots for Mg II and Si IV at three different positions along the linear structure (shown in Figure 3 at 16:12 UT), illustrating the RBE nature of the structure with speeds of -50 km s^{-1} (arrow in Mg II $\lambda-t$; speeds in excess of -50 km s^{-1} for Si IV). See text for discussion.

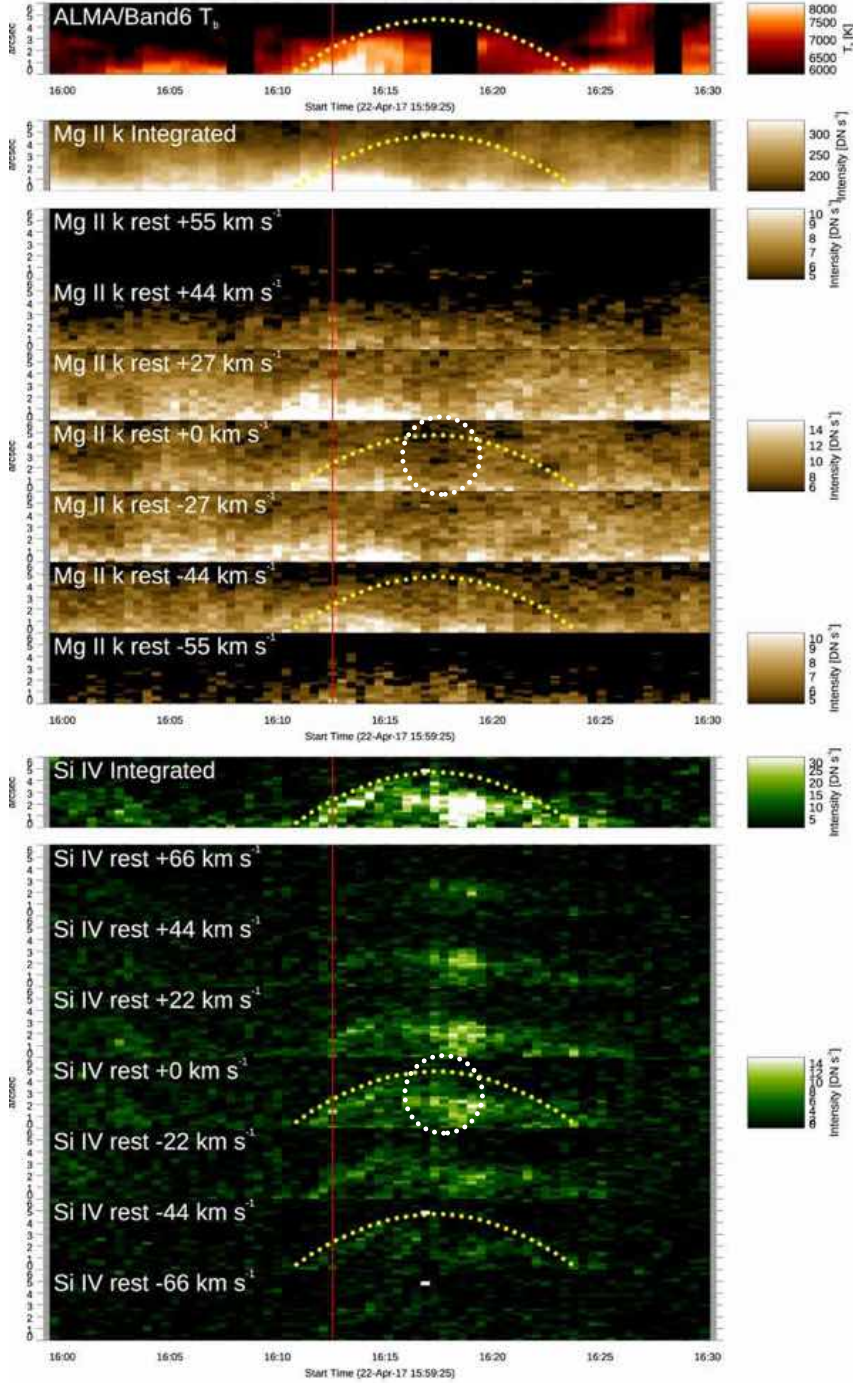


FIG. 5.— *ALMA*/Band6 and *IRIS* raster $x-t$ plots for the linear-like structure shown in Figures 3 and 4. For *IRIS* the stack of $x-t$ plots is arranged in the velocity space as annotated, centered about the rest wavelengths of Mg II k (middle) and Si IV (bottom), in addition to $x-t$ for wavelength-integrated rasters. The west side of the “cut” in Figure 3 is at the bottom of the $x-t$ plots. Note the clear parabolic trace in *ALMA*/Band6 and the wavelength-integrated Si IV $x-t$. Also note the enhanced absorption (dotted circle) in Mg II which alters the appearance of a full parabolic profile. Due to low photon counts in the $x-t$ for Mg II at ± 55 km s⁻¹ we reduce the dynamic range as shown in the respective color bars. The red vertical line denotes the time of observations shown in Figure 4. See text for discussion.

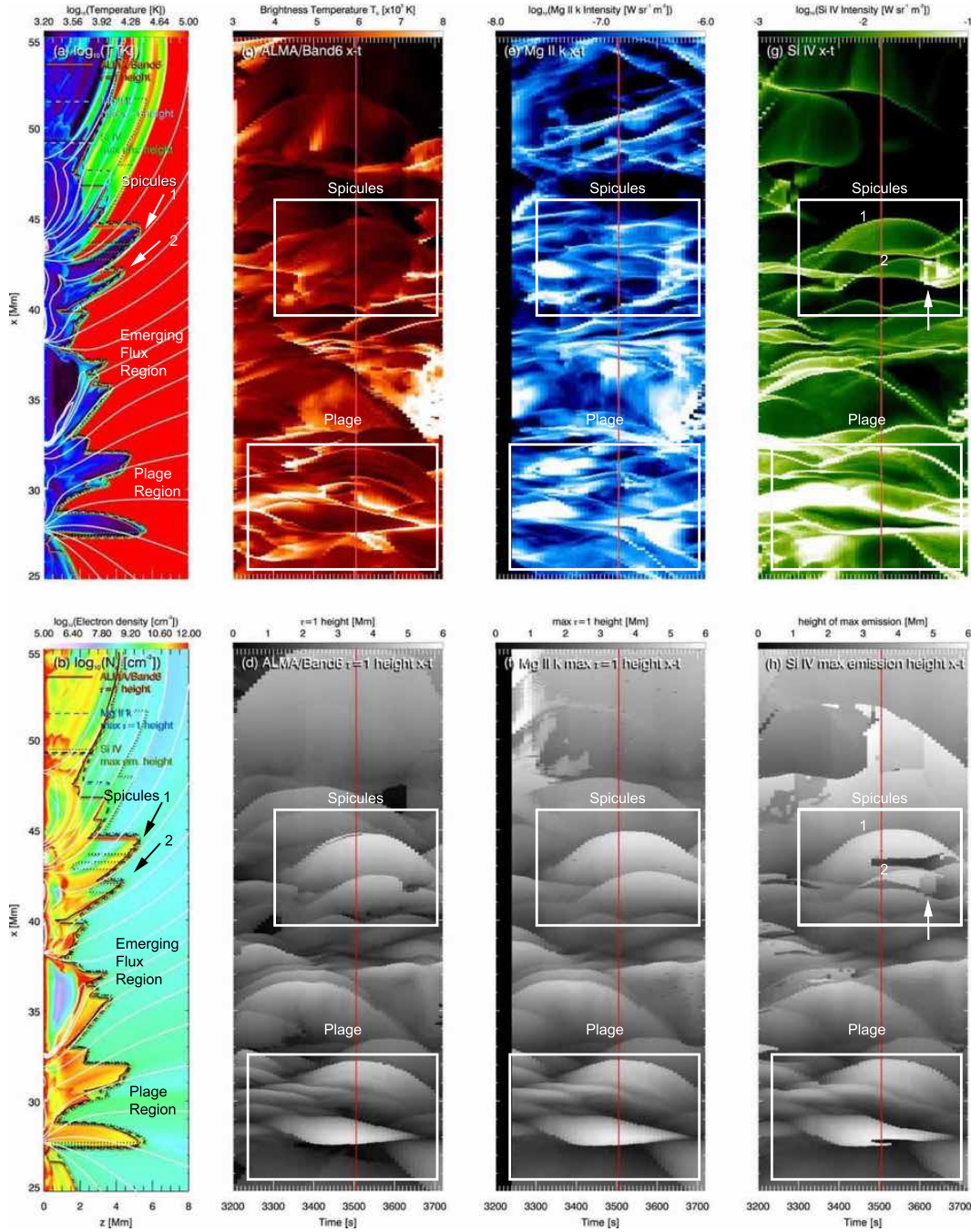


FIG. 6.— Synthetic $x-t$ plots from the Bifrost simulation showing spicules 1 and 2. Left column panels show a snapshot from the simulation at $t=3,500$ s for (a) $\log_{10}T$ and (b) $\log_{10}N_e$. Upper panels (c,e,g) show $x-t$ in *ALMA/Band6* T_b (in red), Mg II k (in blue), and Si IV (in green) synthesized intensities, respectively. Bottom panels (d, f, h) present $x-t$ plots for the geometric height where $\tau = 1$ for *ALMA/Band6*, maximum $\tau = 1$ height for the wavelength-integrated Mg II k, and the height of maximum emission for Si IV. Boxed areas denote the regions of spicules (best seen in Si IV) and plage. With a red line in the $x-t$ plots we mark the time shown in panels (a) and (b).

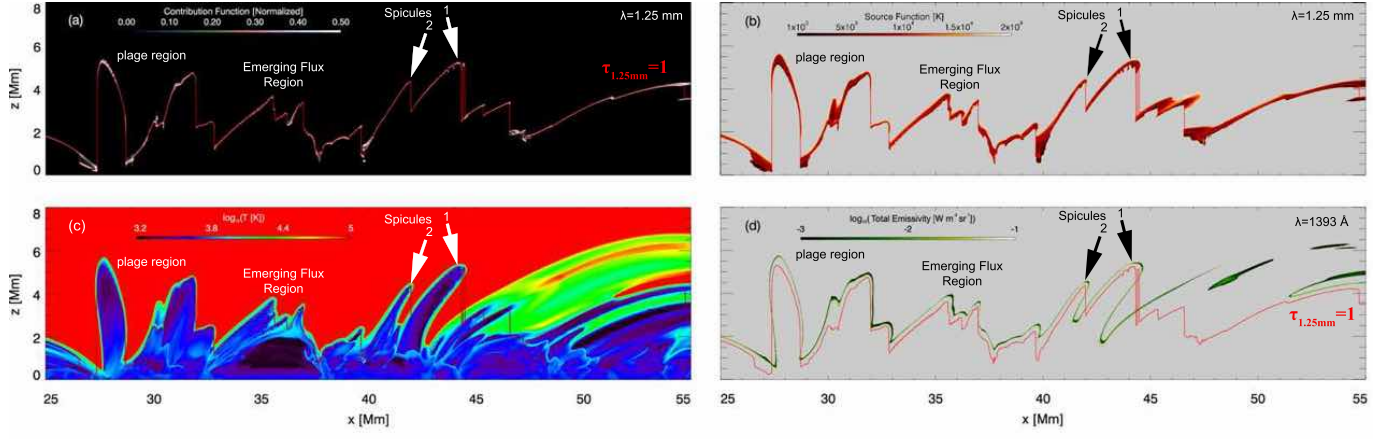


FIG. 7.— *ALMA*/Band6 1.25 mm synthesis from the time of the snapshot of the simulation in Figure 6 of (a) the normalized contribution function (i.e., $g_\nu / \max(g_\nu)$, clipped between 0.0 to 0.5, linear scale) and (b) the related source function, S_ν (here expressed in units of temperature [K] and shown only for regions where $g_\nu / \max(g_\nu) \geq 10^{-4}$; gray mask). The red line in all panels shows the *ALMA*/Band6 $\tau = 1$ height. (c) Temperature map. (d) Color contour (in green; logarithmic scaling; gray mask clipping low values) of the total emissivity, η , for Si IV 1393 Å. Note the close correspondence in the geometric heights for the total emissivity of Si IV 1393 Å and $\tau = 1$ for *ALMA*/Band6 .

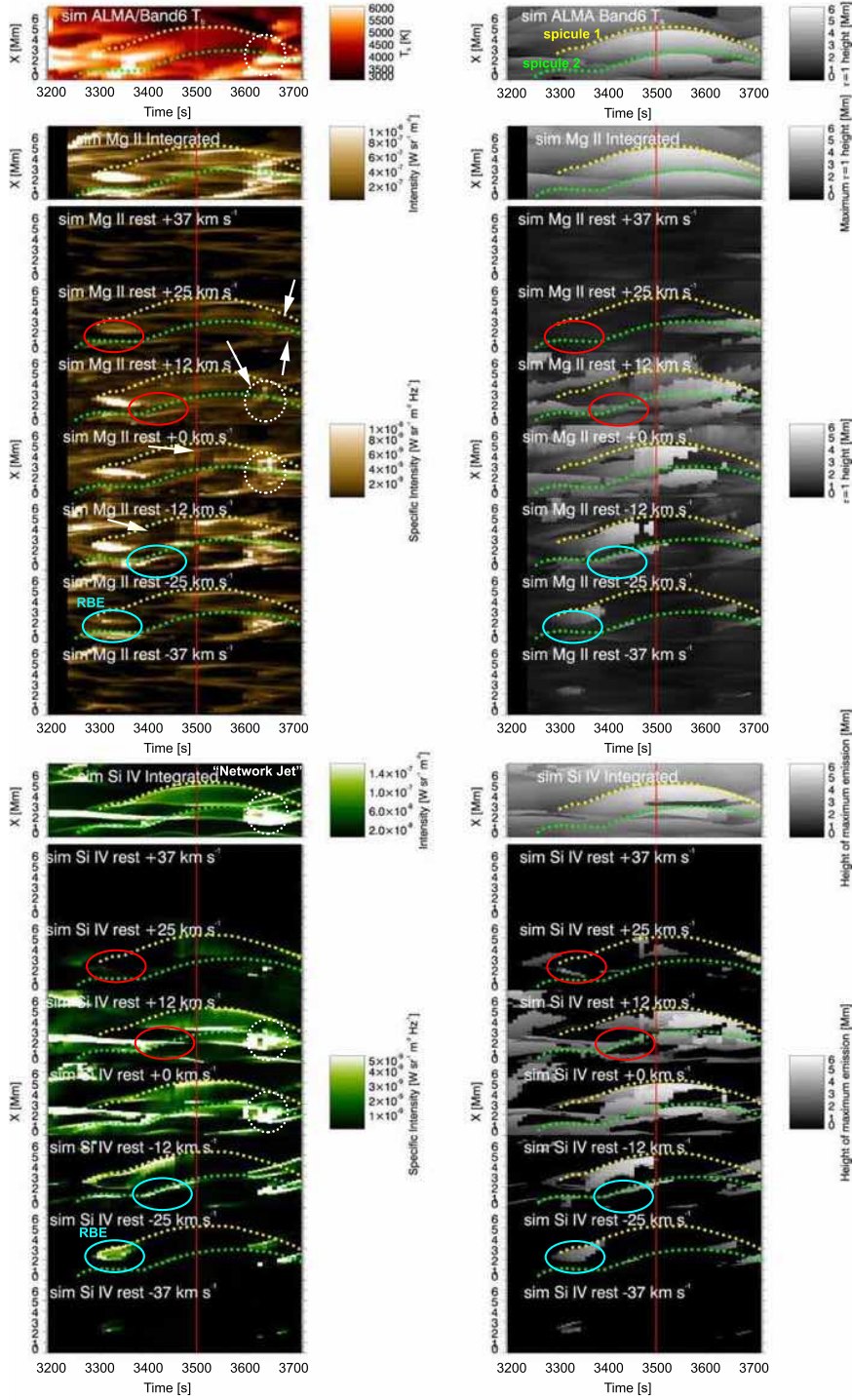


FIG. 8.— Left panels: $x - t$ plots stacked along wavelength (velocity space) for the synthetic observables produced from the simulation. Note the qualitative similarities with the $x - t$ plots produced from the observations (Figure 5). Right panels: $x - t$ plots of the height of maximum emission for the optically-thin Si IV. Dotted lines highlight the parabolic profile of the Type-II spicules 1 and 2 (yellow and green colors, respectively). The arrows show locations of enhanced absorption in Mg II k. The ovals at ± 25 and ± 12 km s⁻¹ pinpoint locations with RBE signatures at the onset of spicule growth. The red vertical line marks the time shown in the previous plots.

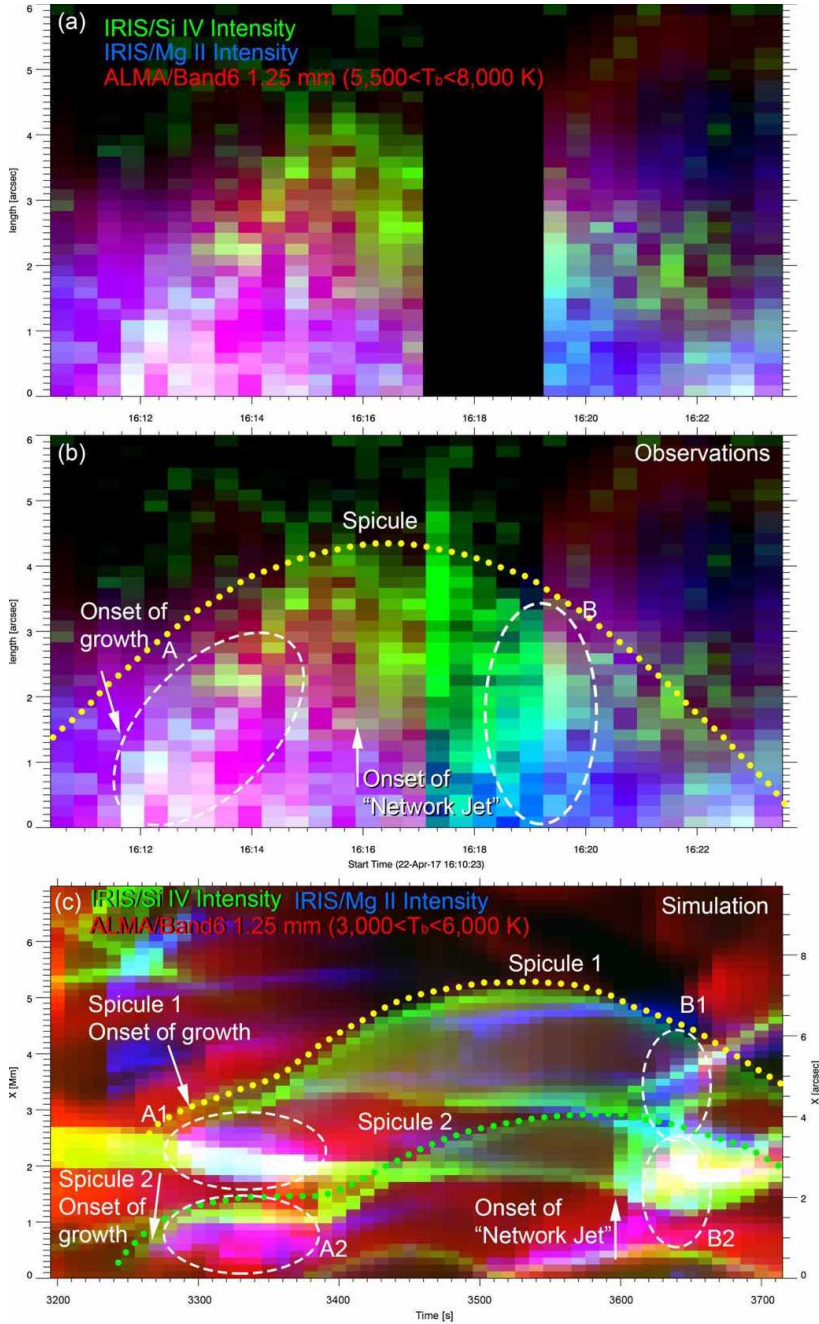
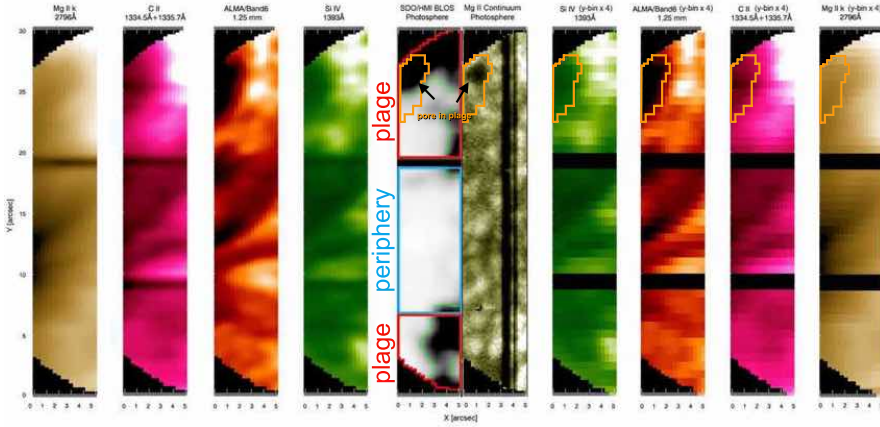
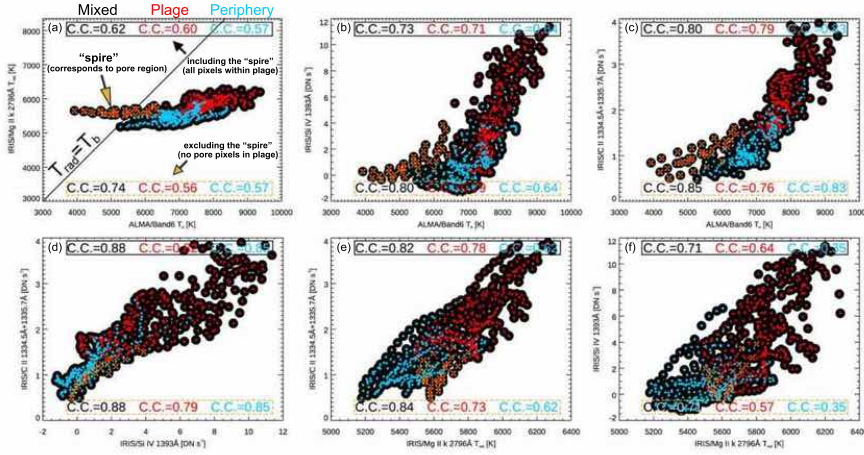


FIG. 9.— Panels (a) and (b): $x-t$ plot combining observations shown in Figure 5 in a tri-color blend: *IRIS* Mg II (blue), Si IV (green) and *ALMA*/Band6 T_b (red). The *IRIS* Mg II and Si IV are integrated along λ covering the line profiles. Panel (a) shows the *ALMA*/Band6 data gap by blocking *IRIS* data. Panel (b) shows the *IRIS* data at all times. Initially the spicule is seen in low temperatures (magenta color blend). The white arrow marks the time of the sudden network jet brightening of the spicule in Si IV (suggesting $T \approx 80,000$ K). Note, however, that at the same time enhanced emission also comes from spicular plasma in lower temperatures (e.g., *ALMA* $T_b \approx 8,000$ K), suggesting that the spicule is a multithermal plasma structure. Panel (c): similar plot from the corresponding synthetic observables for the simulated spicules of Figure 6. See text for discussion.



Scatter plots between time-averaged IRIS and ALMA/Band6 observables



Correlation matrices (excluding pixels above photospheric pore)

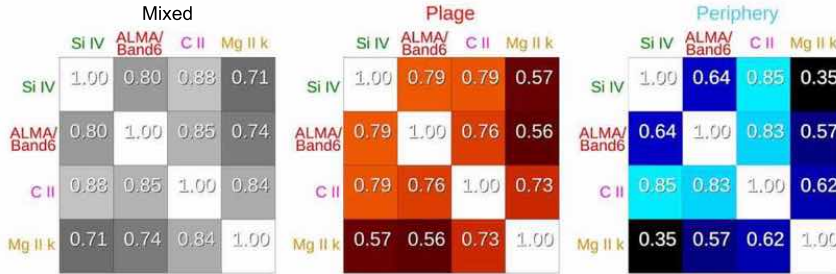


FIG. 10.— Top panels: time-averages of Mg II k (T_{rad}), C II, and Si IV from *IRIS*, and *ALMA*/Band6 (T_b) together with their 4-pixel binned version along slit (y -axis). In the middle we show the time-averaged LOS magnetogram (green contour at ± 100 G) with the subregions considered in the correlation plots (red/plage, blue/periphery of plage) and a Mg II 2832 Å SJI map showing the presence of a photospheric pore in the plage region. Orange contours show pixel area determined as related to the pore, which is excluded in our analysis. Middle panels (a)-(f): Scatter plots for each combination of the 4-pix binned average series. Correlation coefficients (C.C.) are given for (i) points inside the plage area (shown in red), (ii) points inside the area containing the periphery of plage (blue), and (iii) for the entire FOV (black) with and without the pixels in the pore region (top and bottom group of C.C. values, respectively). Note the significantly high correlation between *ALMA*/Band6 and C II and Si IV. Bottom panels: C.C. values excluding the pore pixels organized in correlation matrices. See text for detailed discussion.

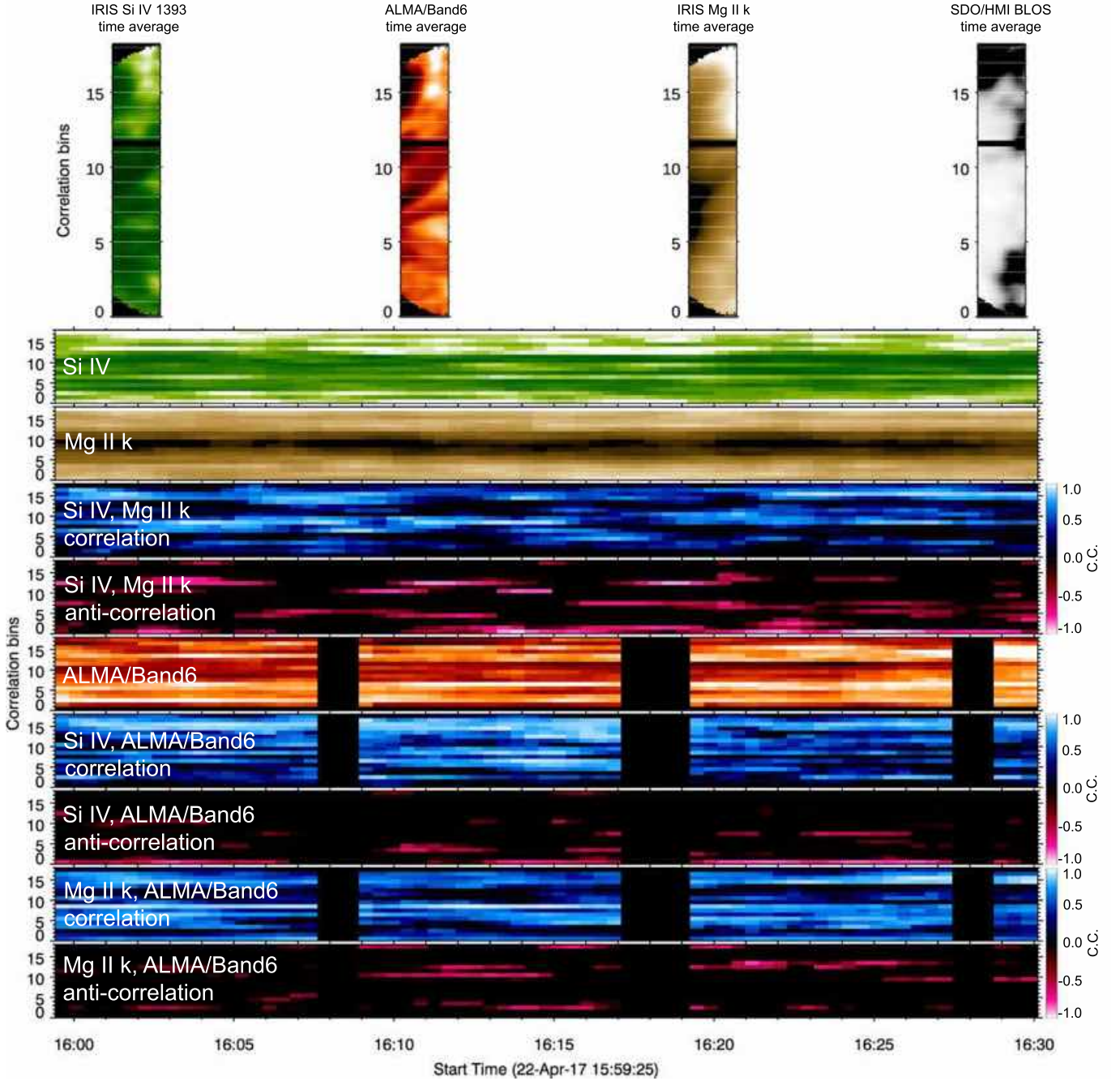


FIG. 11.— Time evolution of correlation and anti-correlation between Mg II, *ALMA*/Band6 and Si IV. The common FOV (covering the center of *ALMA*/Band6 FOV) is segmented into 18 sub regions (correlation bins) covering both magnetic and non-magnetic regions (illustrated with time-averaged maps; top panels). Note that the *IRIS* image raster series has been degraded with the *ALMA*/Band6 beam size and position angle at each individual frame. Bottom panels: For illustration purposes we show the bin-averaged $x - t$ plot for Mg II k, *ALMA*/Band6 and Si IV 1393 Å. Note the clear distinction between areas of moderate-to-high correlation and anti-correlation between Mg II k, Si IV 1393 Å. Note the very high degree of correlation between Si IV 1393 Å and *ALMA*/Band6 across all correlation bins, and the more sporadic distribution of correlation for Mg II k.

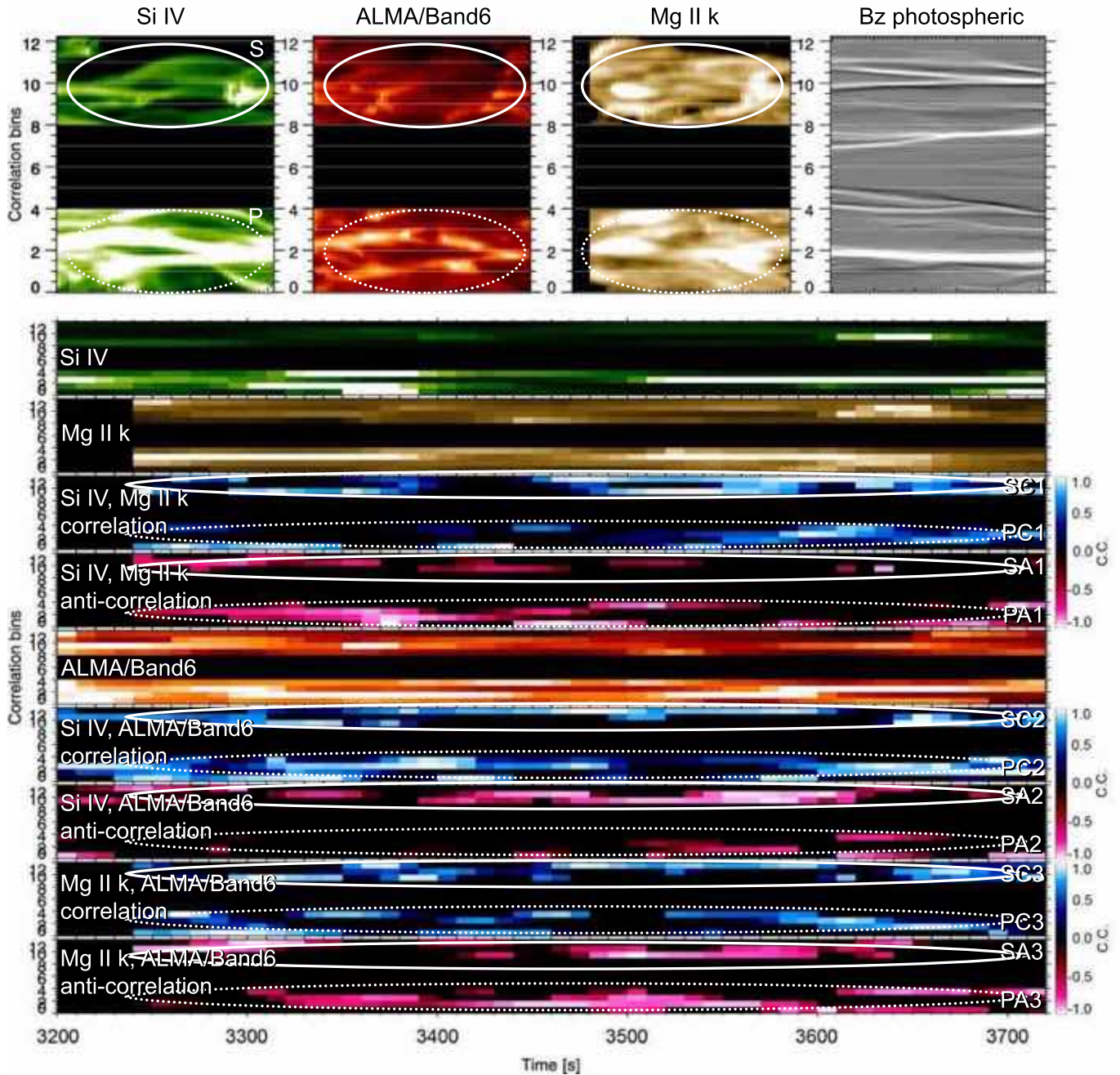


FIG. 12.— Similar as in Figure 11 with analysis method applied on the synthetic observables from the simulation. The spatial resolution in the *IRIS-ALMA* synthetic observables has been degraded accordingly to match the resolution of each observatory and then degraded *IRIS* to match *ALMA* (with an average *ALMA/Band6* beam size of $0''.8$ along the *y*-direction; *x*-direction is the time). The correlation bins have similar physical width across the *y*-direction as with previous Figure 11. The emerging flux region is masked out (blank space) virtually isolating a region of spicules (top region) from a plage region (bottom region). Note the significant spatial extent of persistent anti-correlation between synthetic Mg II k and *ALMA/Band6* observables.

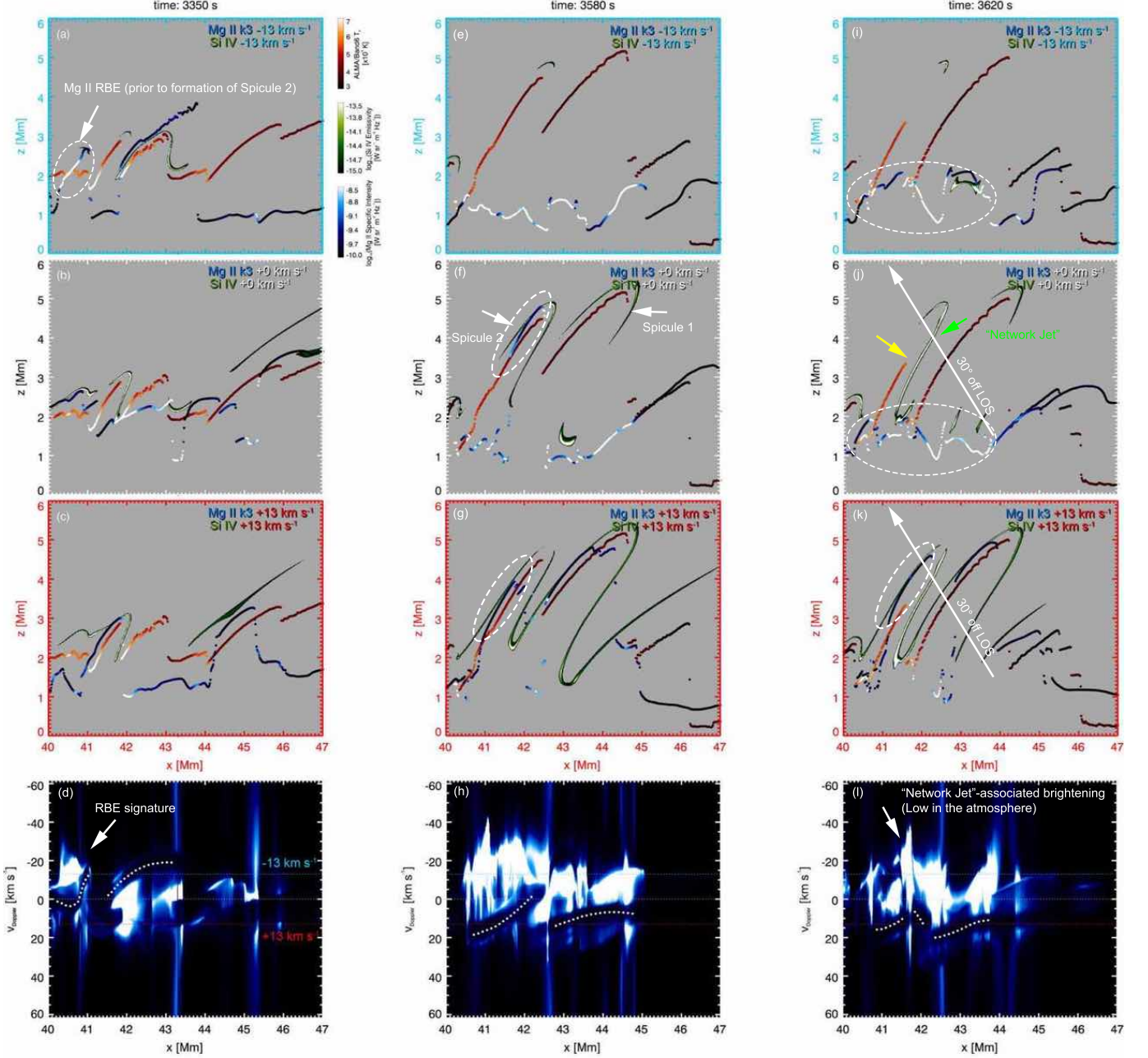


FIG. 13.— Maps from the simulation for the region with the spicules, showing the spatial distribution of *ALMA*/Band6 emission from the spicules (at the height of $\tau = 1$), along with Si IV emissivity and the Mg II k specific intensity (at the height of $\tau = 1$) at three different wavelength positions (corresponding to -13 , 0 , and $+13$ km s^{-1}) and at three different times (one per column). Note that at all times (at least until the brightening of the spicule at $3,620$ s, yellow arrow) *ALMA*/Band6 follows closely the parts of the spicule emitting in Si IV. At $3,620$ s, the brightening occurs when the spicular mass is receding back to the surface, showing significant emission at redshifts ($+13$ km s^{-1}). Bottom row shows the Mg II $\lambda - x$ plot with colored dotted lines denoting the wavelength positions shown above. The dark band seen in the spectra is a well-developed k3 component in Mg II k (parts of it traced by a white dotted line). See text for discussion.

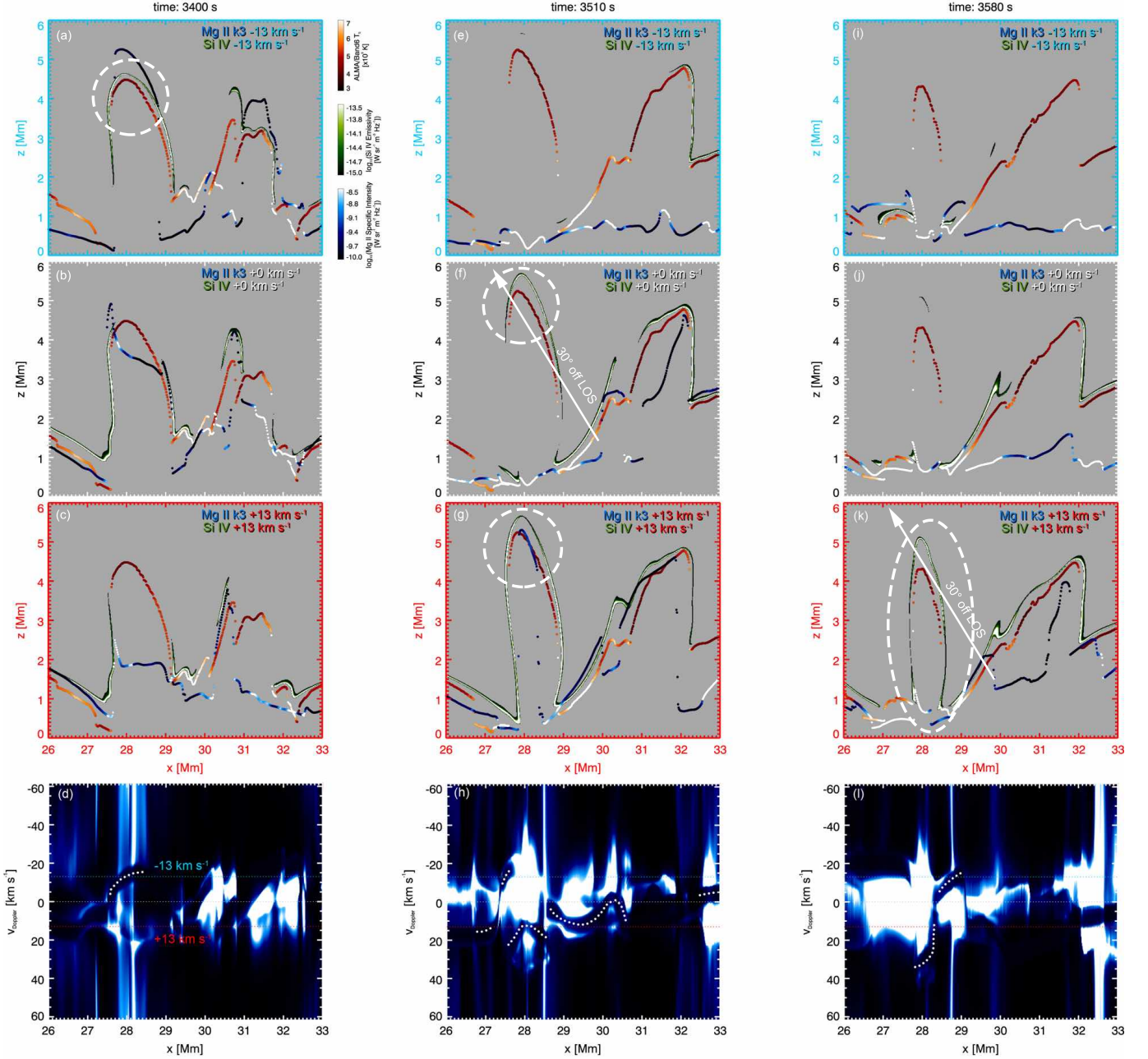


FIG. 14.— Maps from the simulation for the plage region, showing the spatial distribution of *ALMA*/Band6 emission and intensity/emissivity from *IRIS* observables at three different wavelength positions (corresponding to -13 , 0 , and $+13$ km s⁻¹) and at three different times (one per column, as in previous Figure 13). Note that the location of *ALMA*/Band6 emission follows the locations of emissivity in Si IV more closely than Mg II k intensity, which is consistent with the high degree of correlation of *ALMA*/Band6 with Si IV seen in plage regions both in the simulation and in the observations. As in the previous figure, the bottom plots show the Mg II $\lambda - x$ plot with colored dotted lines denoting the wavelength positions shown above. The dark band seen in the spectra is a well-developed k3 component in Mg II k (traced in part by a white dotted line). See text for discussion.

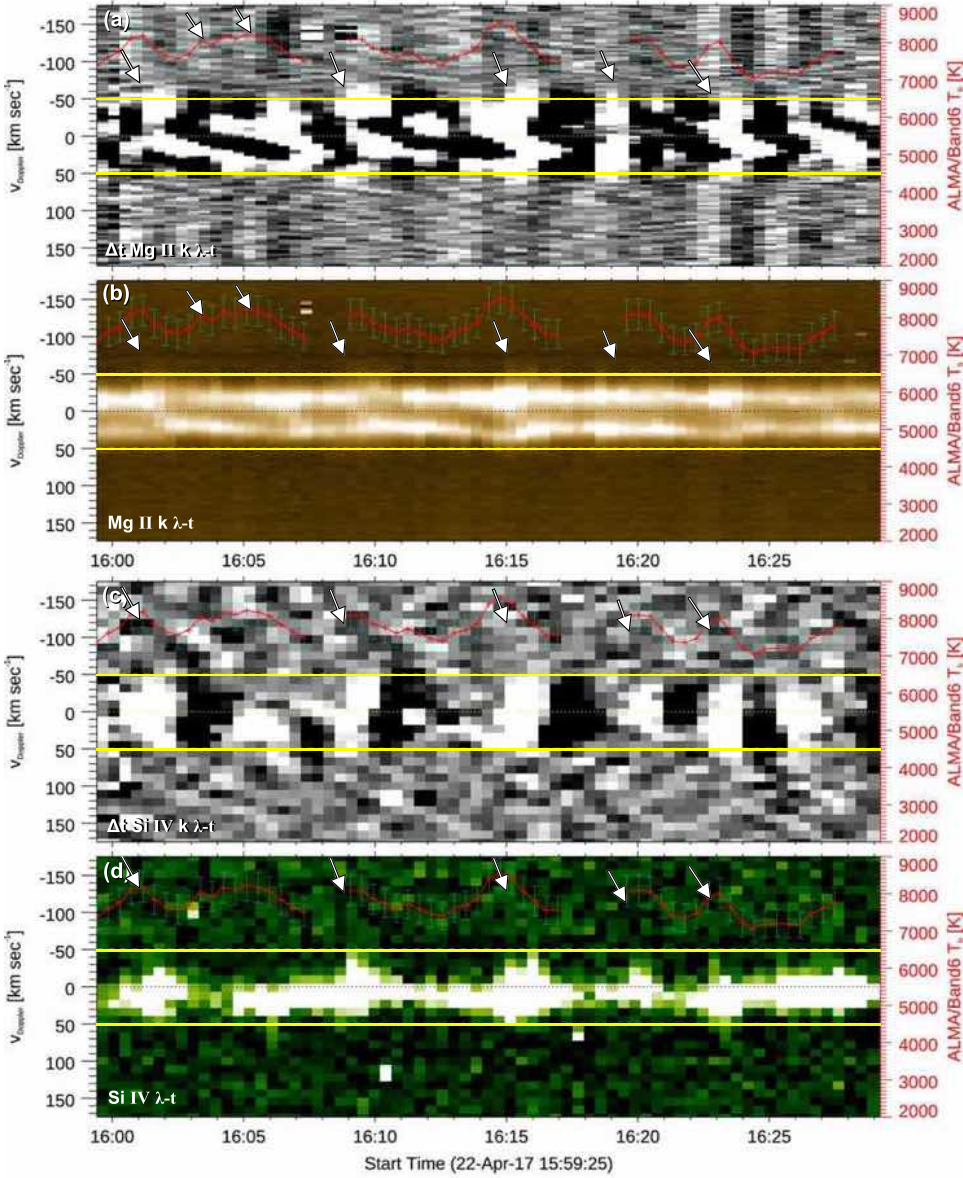


FIG. 15.— Top panels: λ - t plots for Mg II k (b) and its time derivative (a) for the selected $1'' \times 1''$ area above a plage region with recurrent shocks. Bottom panels: Si IV and (d) its corresponding time derivative (c). The λ - t panels are unsharp-masked to improve contrast in the presentation of the figure. In all panels we overplot the *ALMA*/Band6 T_b . The error bars correspond to 5% uncertainty in T_b values. The rest wavelength position is plotted with a dotted line in all panels. Note the correlation of increases in T_b and blue shifts suggesting chromospheric heating due to the passing of shocks in Si IV and Mg II (pointed by arrows).

6. APPENDIX

APPENDIX

To improve the readability of the main text in § 4.2, we host here part of the discussion found in § 4.2.1.2 where we highlight the large discrepancies between our results (and our methodology) with previous studies (e.g., those presented in Bastian et al. 2018; Jafarzadeh et al. 2019). In particular, here we highlight the effects due to the inclusion (or insufficient exclusion) of pores in plage as a source of bias, and we also emphasize our unprecedented time-synchronization between rapid EUV rasters and rapid mm-emission imaging observations in comparison to that achieved by previous studies.

In contrast to Bastian et al. (2018), Jafarzadeh et al. (2019) attempt to remove the pores within the plage by applying a mask derived from an HMI photospheric magnetogram with magnetic field values $\geq \pm 0.8$ kG. However, we note here that the small size of the pores in that plage cannot be fully accounted for by the simple application of a mask from a photospheric magnetogram, due to the natural expansion of fields as they reach chromospheric and transition region heights. Conversely, this makes any pore region mask produced from observations at the photosphere to contain only a part of the associated area higher up, making the safe extraction of pores from the immediate plage a challenging task. This is due to superposition effects and confusion along the line of sight of structures in the chromospheric data. The

definition of pore regions within plage in Jafarzadeh et al. (2019) appears to include real plage signal. In Figures 6 and 7 of Jafarzadeh et al. (2019) we can see that the pore signal is included in the histograms done for other regions in the FOV, namely “Penumbra and Pores”, “Sunspot and Pores”, where the Mg II k2v and k2r and h2v and h2r are clearly skewed to the higher T_{rad} with a sharp drop at 6,000 K. However, the histograms for “Umbra” and “Quiet Regions” are clearly skewed to the low end of T_{rad} with a very gradual drop towards 6,000 K. Thus, they share similarities with the histograms for “Plage”, justifying our concerns for proper characterization of plage from non-plage regions. In our work here, while we are not studying the region above the pore, we are safely excluding it by applying a threshold on $ALMA/Band6 T_b$; this allows to account for the more extended boundaries of structures as they expand from the photosphere to the chromosphere, leaving behind a clean map for plage (Figure 10).

Also, we note that Jafarzadeh et al. (2019) distinguished the $ALMA/Band6$ data into the four sub-bands and only used the one at $\lambda=1.3$ mm, instead of taking the average of all sub-bands as in Bastian et al. (2018) and in our present work. Such averaging results to Band6 maps at $\lambda=1.25$ mm. Finally, Jafarzadeh et al. (2019) strived to take into account the time-differences between the $ALMA/Band6$ mosaic and the scanning time of the large $IRIS$ raster. Unfortunately, due to the nature of the mosaicking scanning process of these particular $ALMA/Band6$ observations (complicated since it does not follow the scanning direction of the $IRIS$ raster, which takes non-trivial amount of time) the authors had only a limited amount of pixels with a minimal time-difference in their dataset. Thus, despite the attempts to match the time between pixels from $ALMA$ and $IRIS$, an adequate amount of pixels for their statistics was obtained with a variable matching of the sampling time, i.e., spanning 0.5-2 min (Figure 4f in Jafarzadeh et al. 2019). In addition, the same work explores correlations between observables by limiting the time-differences to 0.5 min at the expense of sample number. In comparison, Bastian et al. (2018) did not select pixels with such criteria, thus significant chromospheric evolution is not captured in that analysis. As we mentioned in the beginning of § 4.2.1.3, our sampling time synchronization between datasets is superb, i.e., ± 1 s at worst and is consistent throughout the data series analyzed in our work. This is due to the fast $IRIS$ raster scanning times (26 sec) for this particular observation and also thanks to the rapid cadence (2 s) of our $ALMA/Band6$ observations.